Nonlinear Optical Frequency Conversion for Lasers in Space

Diplomarbeit

vorgelegt von

Arne Potreck

am

Institut für Astronomie und Astrophysik,
Eberhard-Karls Universität Tübingen

und

Institut für Technische Physik, Stuttgart
Deutsches Zentrum für Luft- und Raumfahrt e.V.

Juni 2014

Für Andrea Sophie

Contents

Contents

Glossar

ADM   Atmospheric Dynamic Mission
AOM   Acusto-Optical Modulator
AR   Anti-Reflective
BiBO   Bismuth Triborate
CW   Continous Wave
DFG   Difference Frequency Generation
ESA   European Space Agency
FWHM   Full Width at Half Maximum
HLOS   Horizontal Line of Sight
IR   Infrared
KTP   Potassium Titanyl Phosphate
LBO   Lithium Triborate
Lidar   Light Detection And Ranging
LIDT   Laser Induced Damage Threshold
LIC   Laser Induced Contamination
NWP   Numerical Weather Prediction
OFHC   Oxygen-Free High Conductivity
OPO   Optical Parametric Oscillation
PBL   Planetary boundary layer
PID   Proportional-Integral-Derivative
PPM   Parts Per Million
SBS   Stimulated Brillouin Scattering
SFG   Sum Frequency Generation
SHS   Shack-Hartmann sensor
SHG   Second Harmonic Generation
THG   Third Harmonic Generation
UV   Ultraviolet

Deutsche Zusammenfassung

Im Rahmen der Atmospheric Dynamic Mission (ADM)-Aeolous ist der Betrieb eines Lidar (Light detection and ranging)-Systems auf einem Satelliten in der Erdumlaufbahn geplant. Dabei wird ein Laser Pulse vom Satelliten in die Atmosphäre emittieren und anhand der Dopplerverschiebung des rückreflektierten Lichts vertikale Windprofile ermitteln. Das System wird auf einem Nd:YAG-Laser und Verstärker, sowie einer Frequenzkonversionseinheit aus zwei nichtlinearen Kristallen basieren. Mit Letzterer wird die fundamentale Strahlung bei einer Wellenlänge von 1064 nm zu Strahlung bei einer Wellenlänge von 355 nm konvertiert [13]. Für die Frequenzkonversion werden verschiedene Kristalle diskutiert und müssen für den Einsatz im Weltraum qualifiziert werden. Aktuell bevorzugt die ESA ein Design mit zwei Lithium Triborat (LBO) Kristallen [13]. Dagegen wurden in dieser Arbeit die optischen Eigenschaften der Kristalle Kalium Titanylphospat (KTP) und Bismuth Triborat (BiBO) untersucht. Neben der maximal zu errreichenden Konversionseffizienz wurden dabei weitere wichtige Eigenschaften für den Einsatz im Erdorbit untersucht. Basierend auf der Messung der Wellenfrontdeformation eines parallel ausgerichteten HeNe-Lasers, wurde die Ausbildung einer thermischen Linse in situ überprüft. So konnten Absorptionseigenschaften der Kristalle und Veränderungen während der Frequenzkonversion detektiert werden. Weiterhin wurden Langzeittests über 1 % der Missionsdauer durchgeführt. Zur Beurteilung der Kristallqualität wurden laserkalorimetrische Messungen der linearen Absorptionskoeffizienten durchgeführt. Die Arbeit konkludiert durch numerische Simulation der durchgeführten Experimente. Diese zeigt vor allem weitere Möglichkeiten zur Optimierung der Frequenzkonversion auf. Insbesondere die untersuchten BiBO-Kristallen zeigten bei der experimentellen Untersuchung exzellente optische Eigenschaften. So zeichneten sie sich durch geringe lineare Absorptionskoeffizienten (50 ± 10 ppm/cm), stabile Frequenzkonversion unter Langzeitbetrieb (±2 %) und insbesondere eine hohe Konversionseffizienz (48 ± 2 %) für die Generation von ultravioletter Strahlung aus. Damit wurden die Anforderungen der ESA (30 %) und auch die bisher erreichte Konversionseffizienz mit LBO Kristallen (34 %) übertroffen [7]. Bei KTP Kristallen konnte die Ausbildung von Farbzentren in situ detektiert werden und deren Einfluss auf die thermische Linse während eines Langzeitversuches gezeigt werden.

1 Introduction

Weather predictions are based on our knowledge of pressure, temperature, density and wind velocities in the atmosphere [36]. Especially a lack of information on global wind profiles keeps mankind from better understanding the climate system. One of the main goals for future weather satellite missions is therefore to gain precise information on global wind profiles [23]. ESA's Atmospheric Dynamics Mission (ADM)-Aeolus aims to address this lack of information by operating a Lidar (Light Detection And Ranging) system onboard a satellite. The measurement principle is based on a laser system emitting pulses into the atmosphere. From the Doppler shift of the backscattered light and its propagation time through the atmosphere, vertical wind profiles are determined [9].

A dedicated laser system, based on a Nd:YAG oscillator and amplifier operating at a wavelength of 1064 nm, will be used onboard the satellite. To increase the strength of the backscattered signal, the fundamental laser light will be frequency converted to 355 nm. Therefore, a frequency conversion unit, consisting of two nonlinear optical crystals, needs to be qualified and chosen for the space mission [7].

The Diploma thesis focuses on the qualification process for these crystals, within the background provided by the ADM-Aeolus mission. A more detailed description of the mission and the motivation for the frequency conversion onboard ADM-Aeolus is therefore given in Section 2.1 of this thesis. The physical background and the fundamental phenomena of nonlinear optical frequency conversion are explained in the following Section 2.2.

1.1 Nonlinear frequency conversion onboard ADM-Aeolus

Different nonlinear crystals are available and were to be evaluated in regard of conversion efficiency, optical quality and their performance under longterm operation. In the past, experiments with Lithium Triborate crystals (LBO) have been conducted and a frequency conversion unit based on two LBO-crystals is preferred by ESA at the moment [13].

However, the relatively new nonlinear crystal Bismuth Triborate (BiBO) shows higher effective nonlinearities, coupling the electric fields of the fundamental and the converted light, and therefore, could be a promising candidate [32]. Also, Potassium Titanyl Phosphate (KTP) has higher effective nonlinearities than LBO [33]. On the other hand, both crystals have some drawbacks. During longterm operation, absorption centers can form in KTP crystals. The increasing absorption might then influence the conversion efficiency, as well as lead to self-heating of the crystals and consequently to the formation of a thermally induced lens. BiBO is a relatively new crystal and not yet qualified for a space mission. A general drawback could be its smaller temperature and angular acceptance bandwidths.

In Chapter 3, a more detailed insight into the qualification procedure for optics in space and the physical properties of the investigated crystals is given.

1.2 Investigation of frequency conversion

In the course of this work, a dedicated set-up to measure the maximum conversion efficiencies for KTP crystals (which are only suitable for second harmonic generation) and BiBO crystals (second and third harmonic generation) was built. All measurements were performed with the crystals mounted in a holder optimized and suitable for the planned application in space. To verify, if the formation of absorption centers, the so-called gray-tracking occurs, indirect measurements of the thermal lens using a Shack-Hartmann sensor and a co-aligned HeNe laser were performed. Additionally, the temperature distribution on the exit facet of the crystals was measured using an infrared camera.

Longterm stability of conversion efficiency and thermal lensing was investigated with an experiment over 60 million laser pulses, respectively approximately 1 % of

the mission's lifetime. A detailed explanation of the set-up and the conducted experiments is given in Section 4.1, the results are presented in the next Section 4.2. The optical quality of the crystals was investigated and the occurrence of graytracking verified by measuring the linear absorption coefficients in the infrared by laser calorimetry Chapter 5). Additionally, numerical simulations of the conducted experiments were carried out. If simulation matches the experiment, this allows to choose crystals and design an optimized frequency conversion unit. It reveals, whether all processes determining the conversion efficiency are understood and respected in the experiment. The numerical approach and the results are presented in Chapter 6.

In the last chapter, all obtained results are discussed (Chapter 7) and finally the conclusion of the conducted experiments is given (Section 7.2).

2 Background of the Diploma thesis

In this chapter, the ADM-Aeolus mission and its measurement principles, as well as it scientific goals are presented. It is in the course of this satellite mission, that a nonlinear frequency conversion unit needs to be qualified and optimized for an application in space. Therefore, the first section gives a more complete insight into the mission's motivation and its planned technical realization. Since this Diploma thesis focuses on the investigation of possible frequency conversion units for the spaceborne application, the physical background of nonlinear optical frequency conversion is explained in the second section of this chapter.

2.1 The ADM-Aeolus Mission

Understanding the global climate system better and being able to generate precise weather forecasts requires information on global wind systems. Besides temperature, pressure and humidity, it is the wind which plays a key role in our global weather system. However, the established ground-based network to measure vertical wind-profiles in our atmosphere has a limited coverage (e.g. mostly in the Northern Hemisphere). But to understand large scale weather phenomena coupled to atmospheric winds as e.g. El niño, global wind profiles are a crucial information. Especially in the tropics, the wind and the mass field (temperature, density and humidity) are less strongly coupled and independent data assimilation processes become of great importance here [9]. Also, to understand if greenhouse gases affect the global circulation patterns, accurate global wind analysis is necessary. Climate gases, as well as other air pollutions e.g. volcanically generated particles are transported over long distances in the upper troposphere or lower stratosphere through

jet streams. However, measurements from balloons or planes rarely generate wind data from atmospheric layers higher than 20 km and are not feasible on a global scale. ESAs ADM-Aeolus Mission aims to address this lack of information and will demonstrate the capability of a space-based Doppler wind lidar system to measure global wind profiles accurately [9].

The mission is part of ESA's living planet program and ADM-Aeolous will be the first-ever satellite to directly observe global wind-profiles from space [29]. Its active instrument Aladin (Atmospheric LAser Doppler INstrument) consists of a high power laser which emits laser pulses towards the atmosphere at an angle of 35° to nadir, orthogonal to the satellite's ground track velocity vector. The backscattered light is collected with the transmission and receiver telescope and its frequency broadening and shift is measured by interferometry. The Doppler shift and the pulse propagation time allow to conclude on the wind-profiles along the beam line then. In contrast to ground-based measurements of wind-profiles, these spaceborne measurements allow to gain information on wind-formation over the whole globe and increase the measurement accuracy especially in the higher atmospheric layers as troposphere and stratosphere (2-30 km above sea level). Additionally, the signal strength and spectrum of the backscattered signal allows to estimate aerosol and cloud properties in the atmosphere. This addresses one of the major uncertainties in climate change predictions: What is the influence of changes in aerosol and cloud properties in the atmosphere on the radiative balance of the Earth? The global spaceborne measurements will therefore contribute to a better understanding and prediction of the climate change [9].

The satellite is planned to orbit the Earth once every 12 hours at an altitude of 408 km and measure vertical wind profiles of the planetary boundary layer, the troposphere and the lower stratosphere (0-30 km above sea level). A sun-synchronous dusk/dawn orbit was chosen to ensure stable thermal conditions inside the satellite and sufficient illumination of the solar-panels. By pointing the laser-system onto the night-side of the Earth, the solar background is avoided [9].
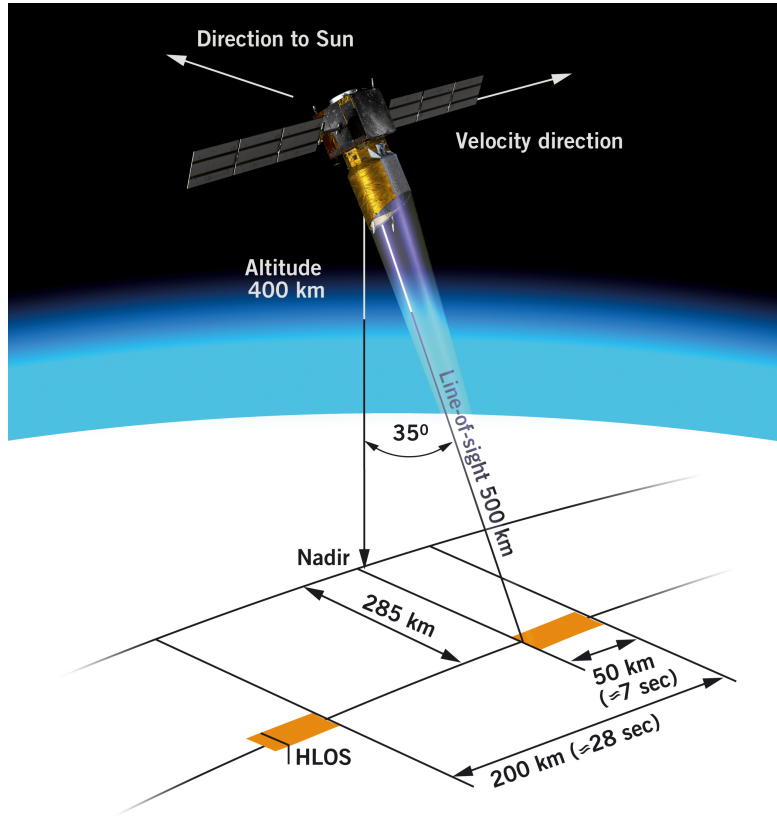
Figure 2.1: ADM-Aeolus and its baseline measurement geometry with the laser pulses shot in an angle of 35° off nadir into the atmosphere and an horizontal line of sight (HLOS) with an observational length of 50 km separated by 200 km [1].

2.1.1 Science

ADM-Aeolous aims to provide exact data on the atmospheric flow to feed Numerical Weather Predictions (NWPs). Hereby, the accuracy of weather reports can be improved and the mission can contribute to a better understanding of our climate system. To substantially improve these simulations, the spaceborne measurement needs to outperform existing measurement methods as ground-based data acquisition and analysis of global winds with e.g. radar measurements.

The underlying method will be to determine the wind velocity by measuring the frequency shift Δf of the emitted laser frequency f_0 due to the Doppler effect.

Table 2.1: Observational requirements of the ADM-Aeolous Mission [9]

| | Observational Requirements | | |
	PBL	Troposphere	Stratosphere
Vertical Domain, km	0-2	2-16	16-30
Vertical Resolution, km	0.5	1	2.5
Horizontal Domain		global	
Number of Profiles, hour^{-1}		100	
Profile Separation, km		200	
Temporal Sampling, hour		12	
Accuracy (Component), m s^{-1}	2	2-3	3-5
Dynamic Range, m s^{-1}		± 150	
Horizontal Integration, km		50	
Length of Observational Data set, year		3	

The shift in frequency is described by $\Delta f = 2f_0 v_{\mathrm{LOS}}/c$ with v_{LOS} the wind velocity along the line of sight (LOS) and c the speed of light. The mission's minimum observational requirements as formulated by ESA are listed in Table 2.1. As mentioned before, the largest impact of the additional spaceborne wind profile measurements will be in the upper troposphere/lower stratosphere. Here the required measurement accuracy to improve NWPs is 2-5 m/s, in the planetary boundary layer (PBL) it needs to be smaller than 2 m/s. This corresponds to a shift in frequency of 11.27 MHz for measurements in the planetary boundary layer (PBL). The required accuracy $\Delta f/f_0$ for the Aladin instrument with its laser frequency f_0 at 844.7 THz is therefore on the order of 10^{-8}. Hence, a spectrally narrow and frequency stabilized laser source is necessary [37]. However, this is a mandatory task for spaceborne lasers, which are exposed to mechanical vibrations and a harsh environment.

To improve global atmospheric analysis, the horizontal density of the measured vertical wind profiles was identified to be of less importance than the accuracy in the measured wind velocity [9]. The mission is aiming for measuring 100 vertical profiles per hour, resulting in 1200 profiles per orbit of the Earth. Aeolus will provide data for numerical weather prediction models, which use average wind data over the resolution grid. Since a grid size of 50×50 km^2 is expected for global NWPs for the next years and data with higher resolution could lead to an

increased uncertainty, Aeolus should ideally deliver data averaged wind profiles over the same grid sizes. Since NWP models have a correlation radius of 200 km, the simulations can become unstable when fed with data with a higher resolution. Hence, the observational length for the Aeolus mission is planned to be 50 km with a spacing of 200 km [13], see also Figure 2.1.

Besides the scientific impact on numerical weather predictions and the contributing to a better understanding of the global climate system, one of the mission's main goals is to demonstrate the possibilities of a spaceborne Doppler wind lidar system. Further on, a successful operation of the Aladin in space paves the way for future technical developments and satellite missions.

2.1.2 The active instrument Aladin

Light will be backscattered in the atmosphere by Mie scattering from aerosols or particles as well as by Rayleigh-Brillouin scattering by single atoms or small molecules. Mie scattering describes the elastic scattering of light with spherical particles and aerosols with diameters D in the range of the scattered wavelength λ ($D \approx \lambda$). In contrast, Rayleigh scattering is the elastic scattering with molecules of $D << \lambda$, for example N_2 and O_2. Additionally, the backscattered spectrum is significantly modified by the inelastic scattering of the laser light with statistical density fluctuations in the atmosphere (Brillouin scattering) [38]. Especially in the stratosphere, the Rayleigh scattering will be dominant since the density of aerosols and particles is decreasing with altitude. However, the molecules backscattered spectrum will be broadened not only by the dispersive movement in the wind but also by the Brownian motion (see Figure 2.2). Consequently, a strong signal in the Rayleigh-regime is needed to get precise information on the wind profile in these atmospheric layers. Since the cross-section for Rayleigh-scattering is strongly dependent on the wavelength (Eq. 2.1, cross-section for Rayleigh-scattering with d: particle size, n: refractive index, λ: wavelength) a laser system with a short wavelength is highly favorable.

$$\sigma_{\mathrm{s}} = \frac{2\pi^5}{3} \frac{d^6}{\lambda^4} \left(\frac{n^2 - 1}{n^2 + 1} \right)^2 \tag{2.1}$$

Besides this, the emission in the ultraviolet was chosen because it is eye safe [9]. The development of the laser system is one of the most challenging tasks of the satellite mission. It has to provide powerful, nearly monochromatic light pulses with high efficiency while being lightweight and cooled only conductively. An additional and demanding task is the long operational time of three years without any possibility of maintenance [14].

For the Aladin Instrument, an established design based on a Nd:YAG-laser was therefore chosen. The laser system consists of a Nd:YAG-oscillator and two amplifiers, the first in double pass and the second in single pass alignment. The fundamental wavelength of the laser system is therefore in the infrared at 1064 nm. By using second harmonic generation followed by sum frequency generation, the fundamental laser light will be frequency converted to 355 nm. The frequency conversion will be done using nonlinear optical crystals especially optimized and chosen for this space-application and long operational time. The laser system will operate at a pulse repetition frequency of 80 Hz with a pulse duration of 30 ns and a spectral width of <30 MHz (FWHM). The pulse energy in the ultraviolet is planned to be 120 mJ (private communication). Improving the frequency conversion efficiency helps to reduce the needed energy of the fundamental laser light and hence helps to reduce the demands on the laser system. A conversion efficiency higher than 30 % is therefore the goal [7].

Wind speeds will be measured over areas of 50×50 km^2 equally spaced by 200 km and it was therefore thought, that the laser system could be switched on every 28 s for 7 s (corresponding to the flight time over the observational length), resulting in a duty cycle of 25 % (see figure 2.1). However, this burst mode would not allow a stable operation of the laser system. Therefore, a continuous operation of the laser system is now planned, resulting in an operational time of approximately 7 billion laser pulses during the missions lifetime of 3 years (private communication). The Aladin system will use a receiving and transmitting Silicon-Carbide light-weight telescope with a diameter of 1.5 m, transmitting the laser signal with a full angle beam divergence of 12 µrad. The receiver will consist of two different spectrometers with a Fizeau interferometer for measurements in the Mie channel and a Double Fabry-Perot interferometer for measurements in the Rayleigh channel. Quasi photon-counting detectors are required to measure the spectrum at low
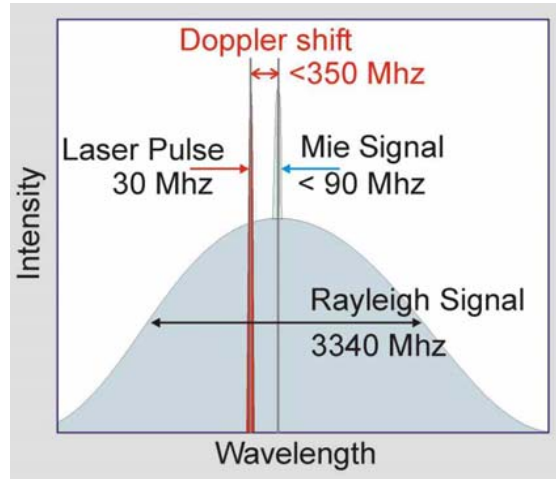
Figure 2.2: Schematic of the spectrum backscattered by Rayleigh and Mie scattering with its Doppler shift and broadening, compared to the spectrum of the outgoing laser pulse, taken from Endemann [13].

noise. CCD's with an on-chip accumulation and high quantum efficiency above 80 % will be used onboard the satellite [13].

2.2 Nonlinear optical frequency conversion

Within this chapter, the physical background of frequency conversion in nonlinear optic material is provided. In the first section, a short introduction is given and the main phenomena are presented. It is followed in the next section by a more detailed explanation of the theoretical background. If not otherwise cited within the text, the insight into nonlinear optics bases on the book "'Nonlinear optics"' by R. Boyd [5] and on book-chapters by E.A.S. Bahaa [3], W. Koechner [22] and D. Meschede [31].

2.2.1 Introduction

The first experimental observation of second harmonic generation of a ruby laser in a quartz crystal was made as early as in 1961 [16]. Since then, conversion efficiencies were subsequently increased and dedicated crystals with high nonlinearities have been found.

Today, nonlinear frequency conversion is a common technique and is widely used to extend the spectrum of high power lasers.

On an atomic level, the nonlinear frequency conversion is based on a perturbation of the electron density due to the interaction of the electrons with the laser radiation. The perturbation creates electric dipoles which for strong incoming electromagnetic fields no longer respond linearly. Hence, they can be a source for scattered radiation at frequencies different to the incoming frequency. On a quantum mechanical level, these distorted electron densities can be calculated in time-independent perturbation theory with a perturbation consisting of a superposition of electric fields at three different frequencies [2]. In plane wave approximation and propagation in z-direction, such an electric field is described by:

$$\vec{E}(z,t) = \sum_{i=1}^{3} \frac{1}{2} \left(\vec{\varepsilon_i}(z) \exp(\mathrm{i}(w_i t - k_i z)) + \text{c.c.} \right) \tag{2.2}$$

whereby ε_i are the amplitudes with polarizations either in x- or in y-direction, ω_i its frequencies, k_i its wavevectors and c.c. the complex conjugated. Within the interaction of two photons at frequencies ω_1 and ω_2, a third photon of frequency $\omega_3 = \omega_1 + \omega_2$ is generated at sum frequency generation. The momentum conservation necessitates:

$$\vec{k_3} = \vec{k_1} + \vec{k_2} \tag{2.3}$$

To understand nonlinear frequency conversion on a more macroscopic scale, one regards the induced polarization in a dielectric medium. Its dependance on the applied electric field $\vec{E}$ in a Taylor expansion is given by:

$$\vec{P} = \epsilon_0 \chi^{(1)} \vec{E} + \epsilon_0 \chi^{(2)} \vec{E}^2 + \dots \tag{2.4}$$

whereby ϵ_0 is the permittivity of free space and $\chi^{1,2,\dots}$ are the linear and respectively the lowest nonlinear susceptibilities. The first term describes the linear response of the polarization to the electric field and is responsible for the basic optical properties such as refraction, dispersion, absorption and birefringence. Usually $\chi^{(1)} >> \chi^{(2)}$ and nonlinear effects are negligible at low electric field strengths, especially when the so-called phase-matching condition (Equation 2.3) is not ful-

filled. In the macroscopic description, phase-matching describes a situation where the interacting waves are coherent over the crystal's length.

Second-order Nonlinearities

It is the second-order susceptibility that couples the electric fields of different frequencies and leads to the nonlinear polarization term $\vec{P}_{\mathrm{NL}}$. It gives rise to the phenomena of sum and difference frequency generation as well as optical parametric oscillation. In a Cartesian coordinate system, the nonlinear polarization can be written as:

$$P_{\mathrm{NL}i} = \epsilon_0 \chi^{(2)}_{ijk} E_j E_k \qquad (2.5)$$

with $i, j, k = 1, 2, 3$. The second-order susceptibility is a tensor of second rank consisting of 27 coefficients. In symmetric crystals or isotropic media it is vanishing and takes place only in noncentrosymmetric or anisotropic media. Due to symmetry reasons, the 27 coefficients can be reduced to 18 independent coefficients and the tensor is usually noted as a 3×6 tensor of first rank, the contracted dielectric tensor d_{ij}. Since physical crystallographic coordinates (a, b, c) are usually not identical with the crystallo-optical axes (X, Y, Z) nor the axes of propagation (x, y, z) of the beam, the nonlinear coefficients must be carefully entered when doing numerical simulation. For fixed propagation and polarization directions, it is possible to reduce the tensor to an effective nonlinear coefficient d_{eff}.

Second and third harmonic generation

In the following, the basic principle of harmonic generation is explained. Hereby, two incoming electric fields at frequencies ω_1 and ω_2 interact in the crystal and a third electric field at frequency ω_3 is generated [22]. We first regard the simplest case of second harmonic generation where the incident electrical field has only one frequency ω_1:

$$E = \varepsilon_1 e^{-i\omega_1 t} + \text{c.c.} \qquad (2.6)$$

This electric field is interacting with the nonlinear polarization (Equation 2.5), which is now given by:

$$P_{\mathrm{NL}} = \epsilon_0 \chi^{(2)} \left(\varepsilon\varepsilon^* + \varepsilon^2 e^{-2i\omega_1 t} + \mathrm{c.c.} \right) \tag{2.7}$$

Hence a first term with frequency zero and a second term at frequency $\omega_2 = 2\omega_1$ results. The nonlinear polarization is therefore a source of the second harmonic of the incident field. The same operation leads, for initial electric field as a superposition of electric fields at two frequencies ω_1 and ω_2, to other terms in the nonlinear polarization. Sum frequency generation is described by a term with frequency $\omega_3 = \omega_1 + \omega_2$, and difference frequency generation is described by a term with frequency $\omega_3 = \omega_1 - \omega_2$. Second harmonic generation is then the simple case of sum frequency generation with $\omega_1 = \omega_2 = \omega$ and $\omega_3 = 2\omega$.

As illustrated with Equation 2.3, the phase-mismatch:

$$\Delta k = k_3 - k_1 - k_2 \tag{2.8}$$

needs to be small in order to realize noticeable frequency generation. For second harmonic generation, for example, this means that $\omega_3 n_3 \approx 2\omega_1 n_1 = \omega_3 n_1$. Since refractive indices are dependent on the wavelength, this is not possible except in birefringent media under interaction of differently polarized waves.

To generate third harmonics one could use four wave mixing with an interaction of the different waves through the cubic susceptibility $\chi^{(3)}$. However, since the cubic nonlinearity is usually very low, third harmonic generation is often done in two steps with second harmonic generation in the first crystal and sum-frequency generation in the second crystal [22].

2.2.2 Theory of harmonic generation

To understand in detail how the nonlinear polarization interacts with the electric field and gives rise to the above named frequency generation, one needs to solve the Maxwell equations in dielectric media with a linear and a nonlinear response

to the electric field. The electric displacement field D is given in such media with:

$$\vec{D} = \epsilon_0 \vec{E} + \vec{P} = \epsilon_0(\chi^{(1)} + 1)\vec{E} + \vec{P}_{\text{NL}} = \epsilon_0\epsilon\vec{E} + \vec{P}_{\text{NL}} \tag{2.9}$$

Equation 2.4 allowed to separate it into a term linear with the electric field $\vec{E}$ and a nonlinear term, the nonlinear polarization $\vec{P}_{\text{NL}}$. From the Maxwell equations one obtains the wave equation in dielectric media:

$$\nabla \times \nabla \times \vec{E} + \frac{1}{c^2}\frac{\partial^2 \vec{E}}{\partial t^2} = -\frac{1}{\epsilon_0 c^2}\frac{\partial^2 \vec{P}}{\partial t^2} \tag{2.10}$$

With the often made assumptions of a loss-less medium without free charges inside the volume ($\nabla\vec{D} = 0$ and $\nabla\vec{E} = 0$) and being nonmagnetic ($\vec{B} = \mu_0 H$), one obtains:

$$-\nabla^2\vec{E} + \frac{1}{c^2}\frac{\partial^2 \vec{E}}{\partial t^2} = -\frac{1}{\epsilon_0 c^2}\frac{\partial^2 \vec{P}}{\partial t^2} \tag{2.11}$$

By separating the polarization into its linear and nonlinear term and substituting Equation 2.9, one finally obtains:

$$-\nabla^2\vec{E} + \frac{\epsilon}{c^2}\frac{\partial^2 \vec{E}}{\partial t^2} = -\frac{1}{\epsilon_0 c^2}\frac{\partial^2 \vec{P}_{\text{NL}}}{\partial t^2} \tag{2.12}$$

The wave equation includes a source term on the right side now. It is the nonlinear polarization, which is the source of the new frequencies. In order to find the truncated differential equations describing the amplitudes of the interacting waves, we start from here. For simplicity, we describe the electric field $\vec{E}$ as a superposition of three monochromatic plane waves traveling in z-direction (Equation 2.2), as well as the nonlinear polarization P_{NL}:

$$\vec{P}_{\text{NL}}(z,t) = \sum_{i=1}^{3} \frac{1}{2}\left(\vec{p}_i(z)\exp(\text{i}(w_i t)) + \text{c.c.}\right) \tag{2.13}$$

When substituting this in the wave equation, it separates into different components for the three frequencies ω_i:

$$-\nabla^2\vec{\varepsilon}_i + \frac{\epsilon\omega_i^2}{c^2}\frac{\partial^2 \vec{\varepsilon}_i}{\partial t^2} = -\frac{\omega_i^2}{\epsilon_0 c^2}\frac{\partial^2 \vec{p}_i}{\partial t^2} \tag{2.14}$$

Solving this differential equation can be simplified with the reasonable assumption of the slowly varying amplitudes. It says that the amplitudes of the waves are slowly changing when compared to the wavelength:

$$\left|\frac{\partial^2 \varepsilon_i}{\partial z^2}\right| << k \left|\frac{\partial \varepsilon_i}{\partial z}\right| \tag{2.15}$$

This leads to some simplifications of the differential operators and results in the differential equations:

$$\frac{d}{dz}\varepsilon_i = \frac{\omega_i^2}{\epsilon_0 c}\frac{i}{2k}p_i e^{-\mathrm{i}kz} \tag{2.16}$$

Coupled equations for three-wave mixing

As we found out (Equation 2.5), the nonlinear polarization couples the electric fields of the different frequencies and mixes them. When substituting the definition of the nonlinear polarization in the differential Equation 2.16, we obtain three coupled differential equations for the amplitudes of the electric fields. They describe the most important second order nonlinear processes, as second harmonic generation (SHG), sum (SFG) and difference frequency generation (DFG) as well as optical parametric oscillation (OPO):

$$\frac{d}{dz}\varepsilon_3 = \frac{2i\omega_3 d_{\mathrm{eff}}}{cn(\omega_3)}\varepsilon_1\varepsilon_2 e^{-\mathrm{i}\Delta kz}$$
$$\frac{d}{dz}\varepsilon_1^* = \frac{-2i\omega_1 d_{\mathrm{eff}}}{cn(\omega_1)}\varepsilon_3^*\varepsilon_2 e^{-\mathrm{i}\Delta kz} \tag{2.17}$$
$$\frac{d}{dz}\varepsilon_2 = \frac{-2i\omega_2 d_{\mathrm{eff}}}{cn(\omega_2)}\varepsilon_1\varepsilon_3^* e^{-\mathrm{i}\Delta kz}$$

At SHG, SFG and DFG one starts with electric fields $\varepsilon_1, \varepsilon_2 \neq 0$ and $\varepsilon_3 = 0$, at OPO with electric fields $\varepsilon_1, \varepsilon_2 = 0$ and $\varepsilon_3 \neq 0$.

Second harmonic generation

We will investigate some of the main phenomena of nonlinear optical frequency generation on the basis of second harmonic generation. Laser light at frequencies

$\omega_1 = \omega_2 = \omega$ enters the crystal, and light at frequency $\omega_3 = 2\omega$ is generated. The three truncated equations reduce to two truncated equations:

$$
\begin{aligned}
\frac{d}{dz}\varepsilon_{\mathrm{SHG}} &= \frac{2i\omega_3 d_{\mathrm{eff}}}{cn(2\omega)}\varepsilon_{\mathrm{FUN}}^2 e^{-i\Delta kz} \\
\frac{d}{dz}\varepsilon_{\mathrm{FUN}} &= 2\frac{i\omega_2 d_{\mathrm{eff}}}{cn(\omega)}\varepsilon_{\mathrm{SHG}}\varepsilon_{\mathrm{FUN}}^* e^{-i\Delta kz}
\end{aligned}
\tag{2.18}
$$

with the amplitude of the electric field of the fundamental wave $\varepsilon_{\mathrm{FUN}}$ and the amplitude of the electric field of the generated second harmonic $\varepsilon_{\mathrm{SHG}}$. In case of small conversion efficiency, the intensity of the fundamental laser light does not significantly decrease over the crystal length l, and the second equation can be approximated to be equal to zero. One simply needs to solve the first differential equation. When solving it analytically, one obtains for the conversion efficiency $\eta = I_{\mathrm{SHG}}/I_{\mathrm{FUN}}$, a sinc^2-function:

$$
\eta = \frac{4d_{\mathrm{eff}}^2\omega^2}{c^3\epsilon_0 n_\omega^2 n_{2\omega}}l^2 I_{\mathrm{FUN}} \cdot \frac{\sin^2(\Delta kl/2)}{(\Delta kl/2)}
\tag{2.19}
$$

By defining the dephasing δ and combining the other variables in one prefactor, the nonlinear drive η_0, a simpler description results:

$$
\eta = \eta_0 \cdot \mathrm{sinc}^2(\delta)
\tag{2.20}
$$

with the dephasing:

$$
\delta := \frac{\Delta k}{2}
\tag{2.21}
$$

and the nonlinear drive:

$$
\eta_0 = \frac{4d_{\mathrm{eff}}^2\omega^2}{c^3\epsilon_0 n_\omega^2 n_{2\omega}}l^2 I_{\mathrm{FUN}}
\tag{2.22}
$$

Conversion efficiency depends on the effective nonlinearity and refractive indices, as well as on crystal length, intensity of the fundamental laser light and on the phase-mismatch Δk. If the phase-mismatch is not vanishing, the conversion efficiency will oscillate over the crystal length, giving rise to the phenomena of conversion and back conversion (see Figure: 2.3). The length of such an oscillation, is the
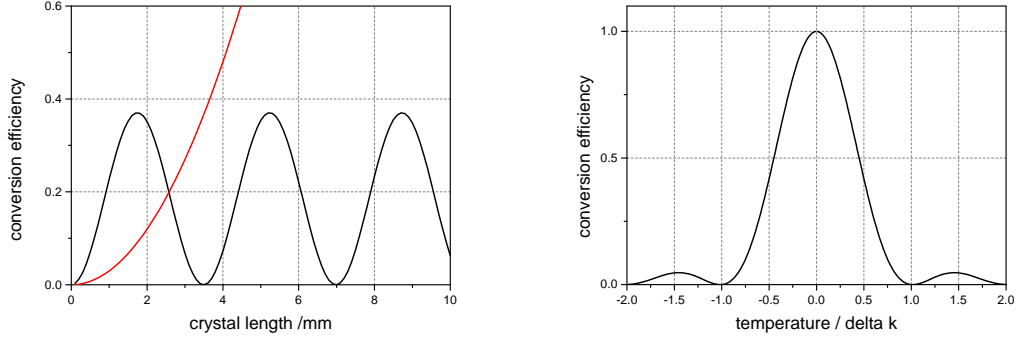
Figure 2.3: Exemplary conversion efficiency vs. crystal length at $\Delta k \neq 0$ (black, with back conversion) and $\Delta k = 0$ (red, without back conversion) on the left side, Temperature bandwidth of BiBO with a sinc^2-behavior and a FWHM of 0.9 K (at THG) on the right

so-called coherence length:

$$l_{\text{coh}} = \frac{\pi}{\Delta k} = \frac{\lambda}{4(n_{2\omega} - n_{\omega})} \tag{2.23}$$

By meeting the phase-matching conditions: $\Delta k \rightarrow 0$, the coherence length approaches infinity $l_{coh} \rightarrow \infty$ and a high conversion efficiency can be realized. Since refractive indices are usually dependent on the wavelength, this is mot possible but in birefringent crystals under interaction of differently polarized waves.

At *type I-phase matching*, the fundamental beam is polarized orthogonal to the generated beam and should be traveling slower through the crystal (s-polarization) than the generated beam (f-polarization)[1]. At *type II-phase matching*, the fundamental beam is partly polarized in s-polarization and partly polarized in f-polarization.

Since the refractive index of a beam, not being ordinary polarized, is dependent on the angle between the optical axes and the direction of propagation, phase-matching ($\Delta k \rightarrow 0$) can be achieved by angle-adjustment of a birefringent crystal. Usually, the nonlinear crystals are not only uniaxial but biaxial, and the phase

---

[1]Since speaking of ordinary and extraordinary polarization in biaxial crystals might not be possible, it is suggested to name a slow polarization (s-polarization) and a fast polarization (f-polarization) [32].

matching angles must be carefully calculated. The crystals are then cut in the specified angles by the supplier, and phase-matching is done through fine adjustment of the crystal's orientation in the beamline. Additionally, the refractive indices depend on the temperature and the calculated angles are valid only for a specified temperature. Phase-matching is therefore possible through angular and temperature adjustment.

Another problem of phase-matching in birefringent media, is the beam walk-off: the direction of propagation of a beam is given by the Poynting vector. For an ordinary beam, the Poynting vector $\vec{S}$ and the wave vector $\vec{k}$ are pointing in the same direction. However, for an extraordinary beam, an angle between wave-vector and Poynting vector results, which is the walk-off angle ρ. S-polarized and f-polarized beams are therefore traveling in slightly different directions through the crystal, not overlapping perfectly anymore. This results in a conversion efficiency which does not depend quadratically on the crystal length l, but only linearly and a generated beam with an elliptical beam profile. Hence, more complex approaches to solve the differential equations analytically, with respect to e.g. the decreasing intensity of the fundamental beam and its propagation through the crystal are necessary and were presented for example by Eimerl et al. [12]:

$$\eta = \eta_m \text{sn}^2 \left[\sqrt{\eta_0/\eta_m}, \eta_m^2 \right] \tag{2.24}$$

with

$$\eta_m = 1 + (\delta^2/2\eta_0) - \sqrt{[1 + (\delta^2/2\eta_0)]^2 - 1} \tag{2.25}$$

where the nonlinear drive η_0 and the dephasing δ are as described before. In contrast to Equation 2.20, the conversion efficiency is now described by a Jacobi elliptic function $\text{sn}(u, m)$. Nevertheless, conversion efficiency is enhanced with an increasing drive e.g. crystal length or laser intensity, until an optimum is reached and the efficiency becomes more and more sensitive to the dephasing δ. Energy is then converted back, and the efficiency cycles with crystal length, as described before [22, 31].

3 Choosing nonlinear crystals for the ADM-Aeolus Mission

In this chapter, the special considerations taken into account for choosing laser optics and especially nonlinear crystals for an application in space, are introduced. Afterwards, the nonlinear crystals KTP, BiBO and LBO, which are considered in this work, are presented. Their basic optical properties are given and their main advantages, as well as drawbacks, are explained. Within this picture, the motivation for the performed experiments is provided.

3.1 Qualification of optics for space applications

To verify optics for the special environment onboard a satellite exposed to extreme conditions, such as vacuum and cosmic radiation, is a demanding task [7]. A stable long term operation of a high power laser system at wavelengths from the infrared to the ultraviolet must be guaranteed for the ADM-Aeolous mission. One of the limiting factors for spaceborne optics is the laser induced damage, possibly occurring on the coated surfaces or in the bulk during laser irradiation with high fluences. Consequently, the damage threshold (LIDT) under vacuum conditions at the specified wavelengths must be determined carefully [39].
Additionally, out-gassing of organic materials onboard the satellite can form deposits on optical surfaces under the influence of ultraviolet laser light. This laser induced contamination (LIC) can alter the optical properties and reduce the damage thresholds of the coatings [43]. Hence, dedicated experiments to measure LIDT and LIC under vacuum conditions are carried out at the Institute of Techni-

cal Physics (DLR). The obtained results must be taken into account when choosing optical elements for a space mission. During the development of the laser system, ESA decided to operate the whole laser system under an artificial atmosphere at a pressure of 40 Pa and 100 % oxygen. In such an atmosphere, experiments showed a reduction of laser induced contamination [14]. This ensures a longer operational time of the laser (private communication). Additionally, the hygroscopy of optical materials might not be a limiting factor under this artificial atmosphere.

Besides these general requirements for space optics, special considerations need to be taken into account when choosing nonlinear optical crystals for the frequency conversion onboard ADM-Aeolus. First of all, the conversion efficiency of the third harmonic generation is aimed to be at a minimum of 30 % [7]. Thus, the crucial point in choosing a nonlinear crystal is the maximum conversion efficiency. Besides this, large temperature and angular acceptance are preferred to account for mechanical vibrations or temperature changes onboard the satellite. According to the agreement with ESA, a phase-matching temperature of 30 °C was chosen for the crystals. Whereby the ambient temperature inside the Aladin instrument will be approximately 20 °C. This phase-matching temperature only 10 °C above ambient temperature, was preferred to reduce the power consumption due to dissipated energy by the crystals. However, a phase-matching temperature which is just slightly above the atmospheric temperature, reduces the possibility to adjust phase-matching through temperature adjustment. Also, it couples the crystal's temperature more directly to the atmospheric conditions inside the Aladin Instrument. Furthermore, absorption centers formed due to the laser irradiation show self-healing only at higher temperatures. Especially for KTP crystals, the formation of this so-called gray-tracking (see Section 3.1.2 for further explanation) might be a limiting factor. To investigate the conversion efficiency under long term operation and the formation of color centers with subsequent heating and induced thermal lensing, long term experiments were carried out in the course of this thesis.

The three non-linear crystals: gray-tracking resistant KTP (KTP_{gr}), BiBO and LBO are potential candidates for the frequency conversion, with LBO crystals being preferred and already characterized. BiBO crystals are relatively new non-linear crystals and not yet completely characterized for spaceborne applications,

KTP crystals are critical because of their formation of absorption centers. Hence, both crystals (KTP and BiBO) were subjects of the experiments performed in the course of this thesis.

3.1.1 Bismuth Triborate

Bismuth Triborate (BiB_3O_6) is a negative biaxial crystal (space group $C2$) consisting of $B_3O_6^{3-}$ rings which form sheets of corner-sharing BO_3^{3-} triangles and BO_4^{5-} tetrahedra in the ratio of 1:2. These anions are linked by six-coordinated bismuth cations in the crystal [34]. It was first described by Levin et al. in 1962 [26], but it took until 1999 to successfully grow crystals with dimensions up to $20\times20\times30$ mm^3 of good optical quality. Hence, BiBO is a relatively new nonlinear optical crystal, the basic optical properties like effective nonlinearities, angular-, temperature- and spectral acceptance bandwidth were not reported until 2006 [50].

BiBO crystals show a high effective second-order nonlinearity d_{eff} exceeding the values of widely established Borate crystals like Beta-Barium Borate (BBO) and Lithium Triborate (LBO) [32]. Being transparent for wavelength between 0.286 and 2.7 μm, it is suitable for a wide range of applications from the ultraviolet to the infrared. A limiting factor for applications in the low ultraviolet could be its bandgap at 270 nm (4.59 eV) [34]. With its high effective nonlinearity and being non-hygroscopic, it is a promising candidate for space missions. A drawback for the planned application in space could be the lower laser induced damage threshold when compared to LBO and KTP crystals. The LIDT, listed in table 3.1, was measured at the Institute of Technical Physics with anti-reflective coated thin-slices of BiBO crystals, provided by the same supplier as the crystals for the frequency conversion experiments. Damage was found on the crystals' coatings and not in the crystals' bulks. Another disadvantage of BiBO crystals could be the smaller angular and temperature acceptance bandwidths when compared to LBO and KTP crystals (see Table 3.1).

In general, BiBO crystals are suitable for second and third harmonic generation, the investigated crystals were a 10.4 mm long crystal for second harmonic generation and a 10 mm long crystal for the following sum frequency generation. Type I phase-matching for both second harmonic and sum frequency generation

were done in the YZ-plane[1] with cutting angles of $\Theta = 12°, \Phi = 90°$ (SHG) and $\Theta = 34.3°, \Phi = 90°$ (SFG). All investigated crystals had entrance and exit facets of 10×10 mm^2.

3.1.2 Potassium Titanyl Phosphate

Potassium Titanyl Phosphate (KTiOPO$_4$) is one of the basic nonlinear crystals and is widely used, already since the 1980s. It finds wide application in second harmonic generation of radiation at a wavelength of 1064 nm, generating harmonics at a wavelength of 532 nm [33]. The crystal is positive bi-axial with point group $mm2$ and shows a high effective nonlinearity d_{eff}, comparable to that of BiBO crystals. Wide temperature and angular acceptance bandwidths allow to realize high conversion efficiencies, not influenced by small temperature variations or mechanical vibrations. This potentially verifies it for an application in space. On the other hand, a few drawbacks of KTP crystals need to be considered. First of all, with its UV transmission cutoff at a wavelength of 350 nm, it can not be used for the generation of harmonics in the ultraviolet [33].

In applications with high peak powers, the performance of KTP crystals is limited by the formation of gray-tracking. Hereby, electron-hole pairs form under the influence of ionizing radiation (e.g. laser light in the visible or ultraviolet, as well as x-rays) and are trapped separately within the lattice. It is suggested that two photon absorption processes at the second harmonic are mainly responsible for this formation of electron-hole pairs. The process leads to the formation of color centers and the absorption increases. This goes along with thermal lensing and harmonic power instabilities. Continued operation at high powers can even lead to the occurrence of catastrophic damage [44]. It was found that the formation of gray-tracking saturates exponentially with laser power and time. The annealing of the color centers takes much longer than the time needed to create the color-centers and the relaxation time decreases by heating the crystal. Above

---

[1]Since the crystallographic axes a, b, c are not necessarily orthogonal in optical material (e.g. in BiBO crystals), an orthogonal right-handed system X, Y, Z was introduced to describe the crystal's orientation and the nonlinear properties like the dielectric tensor. It is fixed to the cristallographic axes by several conventions [40]. Here, the wave is traveling through the crystal in the plane formed by this $Y-$ and $Z-$axes.

100 °C gray-tracking can not even be observed anymore [4]. A lot of effort was taken in the past to identify the process leading to the gray-tracking. When it is identified, so-called anti-gray-tracking crystals can be grown, which could also be of interest for space missions. Since the susceptibility to gray-tracking varies from crystal to crystal and depends on the crystal growth conditions (hydrothermal or flux grown), it is assumed that impurities and vacancies within the lattice are responsible for the gray-tracking formation [4]. An identified mechanism, possibly responsible for the gray tracking, is that Fe^{3+} ions can trap holes (converting to Fe^{4+}) and Ti^{4+} ions located next to oxygen vacancies can trap the electrons (converting to Ti^{3+}) [44]. Efforts were taken in the past to improve the stoechiometry of KTP crystals by modifying the fluxes when growing crystals and by using purer materials, resulting in anti-gray-tracking KTP crystals. In this work, second harmonic generation with such a gray-tracking resistant flux-grown KTP_{gr}-crystal was investigated. Due to the expected slow healing of color centers at the chosen phase-matching temperature of 30 °C, the formation of gray-tracks could still be a limiting factor for the spaceborne application and was to study. The investigated crystal was 9 mm long with type II-phase matching in the XY-Plane at cutting angles of $\Theta = 90°, \Phi = 24.1°$.

3.1.3 Lithium Triborate

The existence of Lithium Triborate (LiB_3O_5) was already found in 1926 by Mazetti and Carli [45]. However, it took until 1989 that the excellent nonlinear properties of LBO crystals were discovered [6]. The LBO crystal is a negative biaxial crystal and, like KTP, it belongs to the point group $mm2$. The crystal structure is based on a large number of anionic boron-oxygen bonds $(B_3O_7)^{5-}$ organized around Lithium (Li^+) cations [45]. It is the anionic group, which is assumed to be responsible for the basic nonlinear properties of Borate crystals as LBO or others e.g. BBO [24]. Because of LBO crystal's high optical damage threshold (for damage in the crystal bulk) and being highly transparent from the near-infrared to the near ultraviolet [49], LBO crystals find wide application in nonlinear optics and are the preferred candidates for the ADM-Aeolus Mission [14]. The damage threshold

Table 3.1: Crystals under investigation, the values for the effective nonlinearities (d_{eff}) were calculated using the free software SNLO by AS-Photonics.

	KTP_{gr}	BiBO (SHG)	BiBO (THG)
phase matching			
type	II	I	I
temperature [°C]	30	56.8	56.8
cutting angle [°]			
Θ	90	12	34.3
Φ	24.1	90	90
length [mm]	9.0	10.4	10
d_{eff} [pm/V]	3.57	3.00	3.89
bandwidths [FWHM]			
angular acceptance ($\Delta\Theta^{int}$) [°cm]	1.82 [15]	0.07 [50]	0.42 [7]
temperature acceptance (ΔT) [Kcm]	24 [15]	2.175 [50]	0.9 [7]
LIDT 10.000 shots [at 3 ns pulse length, in vacuum conditions, for coated thin slices]			
1064 nm [J/cm^2]		10.0±1.5	4.1±0.5
532 nm [J/cm^2]		3.1±0.5	2.5±0.4

of irradiated thin slices at the Institute of Technical Physics was determined to be as high as 35.4±5.1 J/cm^2 at a wavelength of 1064 nm and 10.3±1.5 J/cm^2 at a wavelength of 532 nm (compare with KTP and BiBO crystals in Table 3.1, all damages occurred on the coatings and not in the crystal bulk).

Prior to the investigations of BiBO and KTP crystals during this work, experiments concerning the conversion efficiency and optical qualification were already conducted with LBO crystals at the Institute of Technical Physics. The SHG crystal used in these experiments was cut for type I phase-matching with $\Theta = 90°$ and $\Phi = 10°$, the SFG crystal for type II phase-matching with $\Theta = 44.4°$ and $\Phi = 90°$ [8]. In contrast to KTP and BiBO crystals, LBO crystals show smaller effective nonlinearities (SHG: $d_{eff} = 0.836$, THG: $d_{eff} = 0.52$). However, they show better angular acceptance bandwidths ($\Delta\Theta$, $\Delta\Phi$ for SHG: 4.7/45.9 mrad, for THG: 13.8/2.8 mrad) and temperature acceptance bandwidths than BiBO crystals (SHG: 5.8-6.7 K/cm, THG: 6 K/cm) [33].

In the experiments, the conversion efficiency for second harmonic generation with

an LBO crystal in air was found to be at a maximum of 56 % and for third harmonic generation with the combination of the two LBO crystals was found to be at a maximum of 34 %. The laser system used for these experiments was a Nd:YAG laser (Innoloas Spitlight Hybrid) with pulse length of 10 ns (FWHM) operating at a repetition rate of 100 Hz. The experiments were conducted for divergencies of the fundamental laser beam in between 0.3 to 1.2 mrad. No significant differences in conversion efficiency was found between investigations in air and under vacuum conditions [8].

It was therefore to study in the course of this thesis, if the higher nonlinearities in BiBO and KTP crystals allow for higher conversion efficiencies compared to LBO crystals and if the drawbacks (mainly gray-tracking in KTP crystals and small angular and temperature acceptance in BiBO crystals, as well as lower laser induced damage thresholds) are a limiting factor for the application in space.

4 Frequency conversion experiments

The experimental investigation of conversion performance for the nonlinear crystals KTP and BiBO (at second harmonic generation) and for a combination of two BiBO crystals (at second harmonic plus sum frequency generation) is presented in this chapter. Further on, the basic principle of the longterm experiments is presented and the method to measure thermal lensing in the crystals is explained. A general overview of the test bench is given in the first sections, followed by methods and analysis.

4.1 Experimental set-up

The arrangement of the optical components for the experiments at second harmonic generation is shown in Figure 4.1. The laser pulses, generated with a Nd:YAG laser, pass an optical isolator and a telescope, frequency conversion takes then place in the nonlinear crystal. Afterwards, the beam is split into its fundamental and generated harmonic by the use of two beam samplers in the beamline. The thermal lensing is measured indirectly with a HeNe laser, which is co-aligned but anti-parallel to the Nd:YAG laser. When second harmonic generation takes place, the absorption at the second harmonic leads to thermal lensing in the crystal. This lensing can be determined by measuring the wavefront deformation of the HeNe laser. Herefore, a Shack-Hartmann sensor is used. To gain additional information on the absolute temperatures, the temperature on the exit facet of the crystals was measured with an infrared camera.

A more detailed insight into the experiment and the different components is given in the following paragraphs.
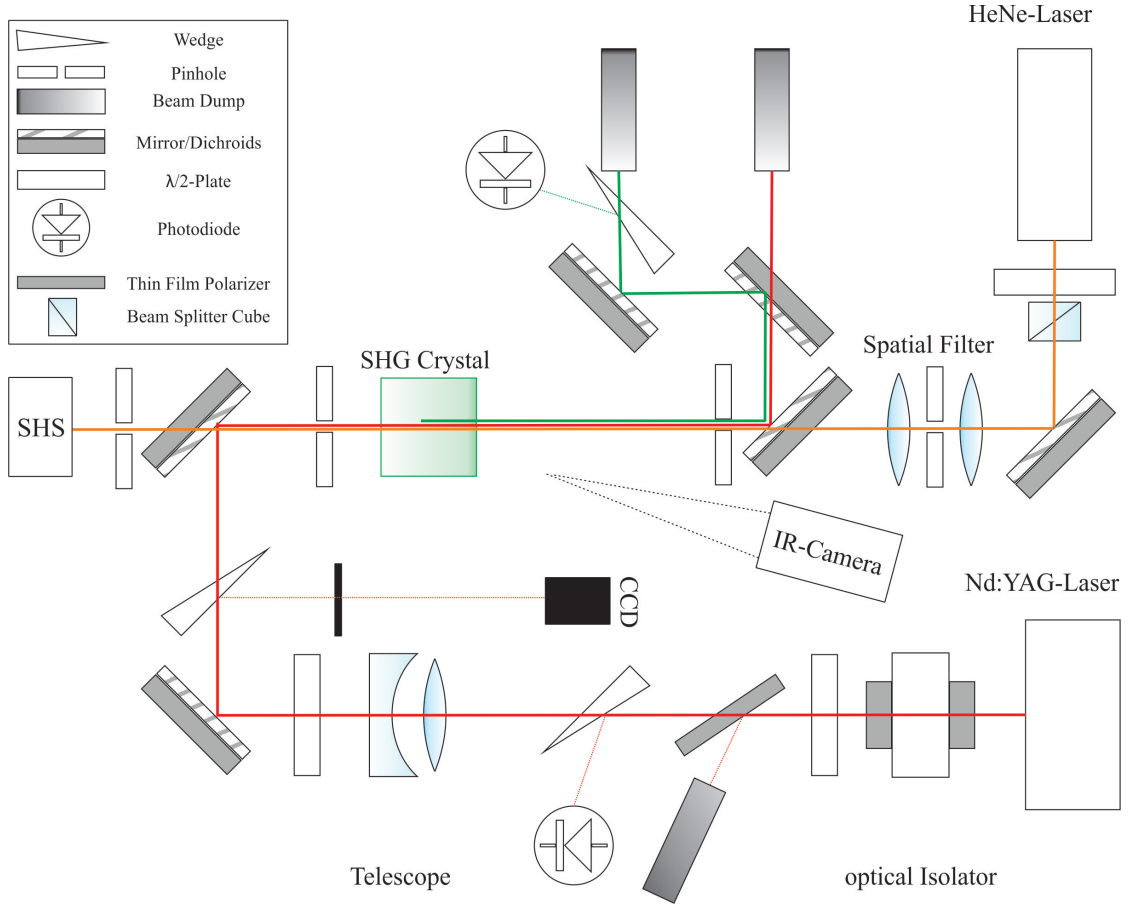
Figure 4.1: Experimental set-up for second harmonic generation with a co-aligned antiparallel HeNe laser for indirect measurements of the wavefront distortion, induced due to absorption in the infrared and the second harmonic inside the crystal.

4.1.1 Second harmonic generation

The Nd:YAG laser provided pulse energies up to 120 mJ at a repetition rate of 100 Hz at the fundamental wavelength. The pulse length was determined to be 4.6 ns (see subsection 4.1.2 for further details on the laser system). The pulse energy was monitored during the experiments using a calibrated pyro-electrical energymeter behind a wedge in the beamline. A telescope in the beamline is used to adjust the beam profile and divergence over the nonlinear crystal's length. Since a collimated beam is needed to reduce losses in conversion efficiency due to dephasing, the beam was collimated by fine adjustment of the telescope. The beamprofile is then
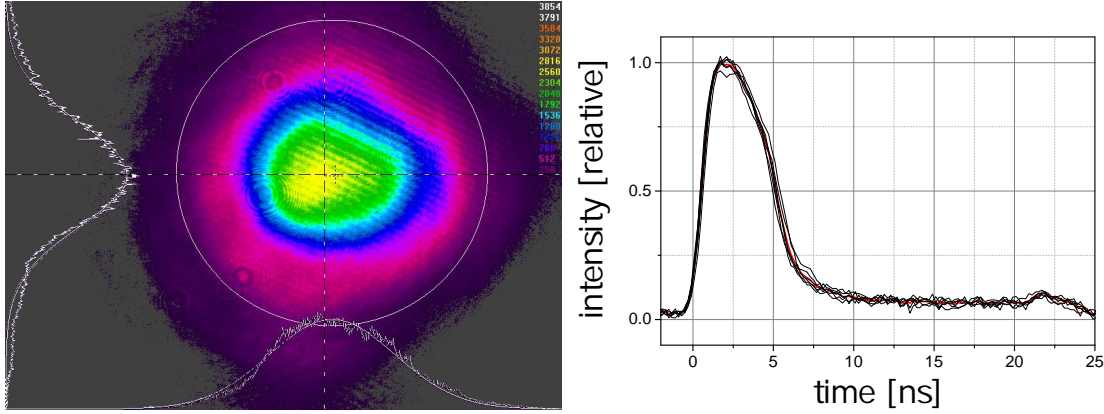
Figure 4.2: Exemplary spatial (on the left) and temporal (on the right) beam profiles on the crystal's entrance facet during frequency conversion experiments for BiBO crystals. A Gaussian spatial beamprofile was suggested and a 2-dimensional fit was applied to the data (left).

controlled with a CCD-beam profiler by Ophir Optronics Solutions Ltd., which is placed behind a wedge in front of the crystal. By moving the camera to the front and back, the beam profile at different levels (e.g. the position of the crystals front facet) can be measured and the maximum fluences as well as the beam's divergence can be calculated.

A Gaussian beam profile was assumed and a 2-dimensional fit was applied to the measured beam profiles. With the derived radius in x- and y-direction at the $1/e^2$-value of the peak intensity, the peak fluences were calculated according to:

$$\text{Fluence} = \frac{2 \cdot \text{PulseEnergy}}{\pi \cdot r_x \cdot r_y} \tag{4.1}$$

Additionally, the polarization of the IR-laser light was adjusted with a half-wave plate in the beamline. Afterwards, the IR-laser beam passes the nonlinear crystal, here the frequency conversion is optimized by angle adjustment of the crystal in the planes perpendicular and horizontal to the beam axes. Behind a mirror being high-reflective coated at the fundamental and its second harmonic wavelength, the beam is split into its two wavelengths. Herefore two beam samplers being high-reflective coated at 532 nm and anti-reflective coated at 1064 nm are used.

The power of the second harmonic is measured directly with a thermal powermeter
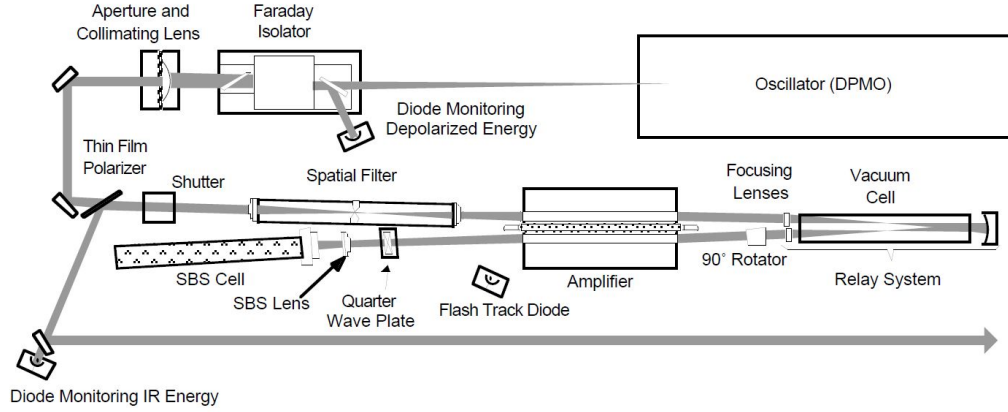
Figure 4.3: Original arrangment of the optical components in the Coherent Infinity^{TM} 40-100 laser system [10], the spatial filter had to be removed due to the occurrence of damage.

or indirectly during long-term investigation by placing a pyro-electrical sensor (for SHG and SHG+SFG with BiBO crystals) or a photodiode (for SHG with the KTP crystal) behind a wedge in the beamline.

4.1.2 Infrared-Lasersystem

A Coherent Infinity^{TM} 40-100 system was used as infrared laser source. The Q-switched Nd:YAG master oscillator and double pass amplifier design provides pulse energies up to 200 mJ at 100 Hz and 3.5 ns (FWHM) pulse duration.

The master oscillator is pumped by a diode laser and consists of a Nd:YAG rod in a ring resonator. An acusto-optical modulator (AOM) inside the resonator serves as Q-switch, allowing to generate high energy and nanosecond pulses when the AOM is turned off and the quality of the resonator abruptly increases.

Afterward, the pulses pass an optical amplifier consisting of two flash-lamp pumped Nd:YAG rods. Using a double pass configuration of the two rods, allows to operate them at small signal gain in the first pass and at saturation in the second pass. To suppress the amplification of spontaneous emission and increase the beam quality, a vacuum spatial filter and a stimulated Brillouin scattering cell (SBS-cell) are introduced in the beam line. In this set-up, the SBS-cell is used as a phase-conjugate mirror helping to correct wave-front distortion accumulated during first

and second pass of the amplifier. A thin film polarizer is used to couple light out of the amplifier. The alignment of the optical components in the laser system is shown in Figure 4.3.

Due to the occurrence of laser induced damage on the spatial filter, the whole vacuum cell with lenses and pinhole was removed. Additional damages on the thin-film polarizer made an exchange and hence a new alignment of the laser beam inside the amplifier necessary. However, the high beam quality in the TEM_{00}-mode with an excellent Gaussian beam profile and M^2 less than 1.5 as stated in the manual could not be reproduced. The pulse length of the used laser system was measured with a fast photo diode to be 4.5±0.3 ns instead of the nominal 3.5 ns stated in the manual (Figure 4.2).

4.1.3 Mounting of the crystals

A mount design, dedicated for the operation in space, was designed at the Institute of Technical Physics (DLR). It consists of a crystal holder, fabricated out of Oxygen-free high thermal conductivity (OFHC) copper, mounted on a Macor base-plate (see Figure 4.4). To reduce thermal losses by radiation, a thin gold coating was applied on the crystal holder. The thermal contact between crystal and crystal holder is improved by placing a thin indium foil between them. The mount was designed to ensure stable operation by securely fixing the crystal without the use of any out-gassing organic materials like glue.

Heating and temperature control of the crystal holders is done with two resistive heaters of 9.6 Ω and a Proportional-Integral-Derivative (PID)-controller (Eurotherm 2408). In a first step, power consumption was measured and the voltage on the heaters chosen to match this power consumption. This optimizes the on-duty time of the PID controller (near 100 %) and helps to stabilize the temperature control over time. The proportional, integral and derivative gain of the PID controller were then determined by the auto-tuning algorithm of the controller. To verify if the crystals are spatially homogeneously heated, simulations of the heat transport were done. Therefore the finite element program by Ansys Inc. was used. The simulation was followed by the experimental investigation with an infrared-camera. Also. the temperature stability over time was controlled with the IR-camera.
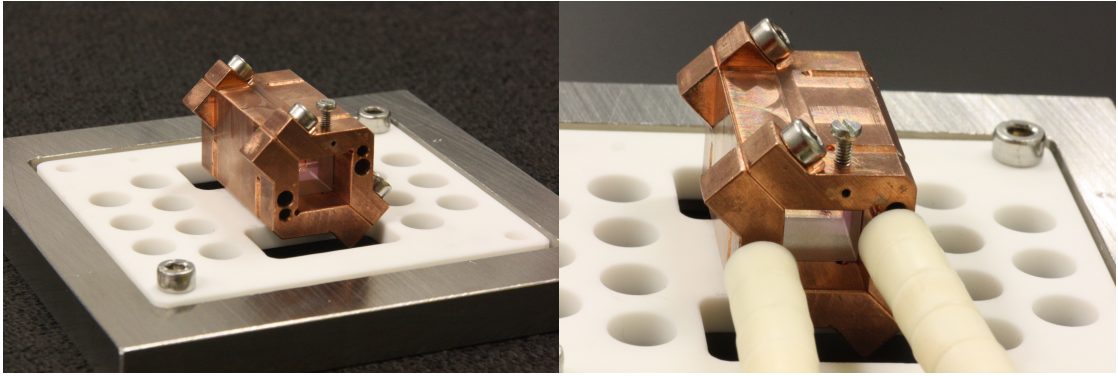
Figure 4.4: NLO-mount design for applications in space consisting of an OFHC-crystal holder and a Macor baseplate. Heating is done with two resistive heaters (right).

4.1.4 Monitoring of the crystal's temperature

The FLIR Inc. T420 infrared-camera was used to measure temperature profiles on the crystals' facets. The temporal and spatial profiles of surface temperatures allows to gain information on the formation of color centers as well as on temperature gradients, which itself could influence the conversion efficiency.

The camera is based on a microbolometer array with 320×240 pixels, has a temperature range of 252 K to 1022 K and a thermal sensitivity of 45 mK. A transmission spectroscopy of the crystals showed that all investigated crystals are not transmissive (transmissivity less than 0.012) for the wavelengths the camera is sensitive for (7.5-13 μm). Hence, only information on the crstals' surface temperatures is accessible with the IR-camera. Since the camera can not be placed directly behind the crystal and inside the high power laser beam, the camera was placed at a slight angle of view in a distance of approx. 70 cm to the crystal. Hereby, a loss in optical resolution of the crystal's exit facet results. During second harmonic generation, the resolution on the exit facet was 37×37 pixels, resulting in 0.27×0.27 mm^2 per pixel.

Before the measurement of the surface temperatures, the ambient temperature and background scattering were measured and entered in the camera settings. To determine the emissivity of the crystals, the mount was heated to different temperatures. When the temperature of the mount has stabilized at a given temperature,

the crystal temperature is measured with the infrared-camera and the mount's temperature with a thermoelement. A homogenous heating was suggested and the emissivity adjusted, so that IR-measurement matches the direct measurement of the mount temperature. By repeating this procedure for different temperatures, the emissivity for KTP_{gr} crystals was found to be $\epsilon = 0.65\pm0.03$ and for BiBO crystals, it was found to be $\epsilon = 0.68\pm0.03$.

4.1.5 Wavefront measurements

A common way to gain information on the development of absorption centers in situ is the use of a probe beam, co-aligned with the test beam. For example, Boulanger et. al. [4] used a HeNe laser split into two beams of which only one passed the crystal. The difference in intensity of the two beams over time allowed to conclude on changes in absorption. In this Diploma thesis, another approach to monitor changes in the absorption was chosen and will be described in the following.

Also here, a frequency stabilized HeNe laser beam passed a spatial filter and was then co-aligned with the Nd:YAG laser beam. Together they passed the nonlinear crystals. But in contrast to the above explained approach, not the intensity of the HeNe laser was measured. Instead, the wavefront deformation caused by absorption of the Nd:YAG laser beam in the crystal and the resulting heating of the crystal was measured. This allows not only to gain information on absorption, but also on its resulting thermal lensing and focusing of the beam. Especially an increasing focusing over time could be a limiting factor for an application in space. The measured wavefront depends on the optical path length τ, which the HeNe laser experiences in the crystal. When the crystal is heated, this optical path length changes. If heating is not homogenous, e.g. because of the Gaussian profile of the Nd:YAG laser, a wavefront deformation results. In contrast to the measurement of the crystal's surface temperature with the IR-camera, the changes in optical path length $\Delta\tau$ can be caused by temperature changes over the whole crystal length.

Three processes play a role for changes in optical path length due to heating: change of refractive indices Δn_{th} due to the temperature change, thermal expan-

sion ΔL_{th} and strain Δn_{st}. The change in optical path length $\Delta\tau(r)$ through the crystal's length L at a given radial distance r from the Nd:YAG laser beam's center is therefore given by [28]:

$$\Delta\tau(r) = \Delta n_{\text{th}}L + n_0\Delta L_{\text{th}} + \Delta n_{\text{st}}L \tag{4.2}$$

Whereby the dominating effect is the change in refractive index, as Mansell et al. [28] showed for different optical materials (e.g. the nonlinear crystal LiNbO$_3$). If heating was homogenous over the crystal length L, this would lead to:

$$\Delta\tau(r) = L\frac{\partial n}{\partial T}\Delta T(r) := c\Delta T(r) \tag{4.3}$$

Where ΔT describes the change in temperature, and $\frac{\partial n}{\partial T}$ describes the linear dependency of the refractive index on the temperature. The latter and the crystal length L can be reduced to the constant c. However, this is valid, only if absorption of the infrared laser light and heating of the crystal is homogenous over the crystal length. But this is not the case for the investigated nonlinear crystals under harmonic generation. Absorption coefficients at the different harmonics vary, as well as the intensities of the harmonics vary over the crystal length. Finally, gray-tracking in KTP crystals is driven by two-photon absorption of the second harmonic (see section 3.1.2). Hence, the introduced absorption centers are not distributed homogeneously over the crystals length. Consequently, an integration of optical path length changes over the crystal length is necessary:

$$\Delta\tau(r) = \int_0^L \frac{\partial n}{\partial T}\delta T(z,r)\,\mathrm{d}z \tag{4.4}$$

The temperature dependence of the refractive indices for the investigated crystals are given with the temperature dependent Sellmeier equations [19, 48]. In contrast, to gain information on the temperature distribution within the crystal $\delta T(z,r)$ is a delicate problem. It is described by the heat equation [28]:

$$\nabla^2 T + \frac{Q}{k_{\text{th}}} = \frac{1}{D_{\text{th}}}\frac{\partial T}{\partial t} \tag{4.5}$$

for a heat source density Q, a thermal conductivity k_{th} and a thermal diffusivity D_{th}. An analytical solution for the heat equation is given with the assumptions of a Gaussian beam profile for the heat source and that heat transport is only radial with the sample being much larger than the heated area [46]. The assumption that heat is only transported radially is critical, if the temperature gradient over the crystal's length is dominating over the radial temperature gradient. Since this is not the case and the crystal is in excellent thermal contact with the crystal holder, this assumption was valid. The analytical solution is then given by [46]:

$$\delta T(r,z) = \frac{\alpha(z,\lambda)P(z,\lambda)}{4\pi k_{\mathrm{th}}} \left[\sum_{n=0}^{\infty} \frac{(-1)^n \left(2\frac{r^2}{w^2}\right)^n}{n \cdot n!} \right] \tag{4.6}$$

with the absorption coefficient α, the laser power P and w the $1/e^2$-radius of the Gaussian beam. To describe the thermally induced lens, the magnitude of the radial thermal difference is introduced [28]:

$$\delta T_{\mathrm{mag}}(z) := |\delta T(0,z) - \delta T(w,z)| = 0.105 \frac{\alpha(z,\lambda)P(z,\lambda)}{k_{\mathrm{th}}} \tag{4.7}$$

It describes the temperature difference between the temperature at the center of the beam and at the $1/e^2$-radius. Following the definition of $\delta T_{\mathrm{mag}}(z)$, the magnitude of the thermally induced lens is defined by: $\Delta\tau_{\mathrm{mag}} := |\Delta\tau(0) - \Delta\tau(w)|$. With Equation 4.4 and substituting of Equation 4.7, it is now given by:

$$\begin{aligned} \Delta\tau_{\mathrm{mag}} &= \int_0^L \frac{\partial n}{\partial T} \delta T_{\mathrm{mag}}(z)\, \mathrm{d}z \\ &= \frac{0.105}{k_{\mathrm{th}}} \int_0^L \sum_{\lambda} \frac{\partial n(\lambda)}{\partial T} \alpha(z,\lambda)P(z,\lambda)\, \mathrm{d}z \end{aligned} \tag{4.8}$$

When no frequency generation is taking place, the summation over the different wavelengths and absorption coefficients is not necessary. Also the laser power is not significantly changing over the crystal length. In this case, summation and integration are not necessary and the magnitude of the thermally induced lens $\Delta\tau_{\mathrm{mag}}$ is directly proportional to the absorption coefficient. By calibrating the system with laser calorimetry (see chapter 5) or other techniques, even absolute

absorption measurements are possible [53]. Changes in the wavefront distortion over time lead directly to changes in the absorption coefficients and to information on optical aging[1], bulk damage or gray-tracking. Another approach would be to scan the optics with a HeNe laser aligned perpendicular to the Nd:YAG laser beam. The integration of the varying laser intensity over the crystal length becomes obsolete then. However, the available crystals were not polished on the side facets. Our aim was not to establish new methods for absorption measurements but to investigate, if the crystals show gray-tracking, gradual heating and thermal lensing during frequency conversion. The absolute values of the absorption coefficients were determined by the established laser calorimetry (see Chapter 5). Work was first started on a Jedi-laser system by Thales Inc. Due to a failure in the laser system, time was spent on getting the experiments started again and maintaining the laser system. However, the above named determination of absolute absorption coefficients could be a follow-up project. In this work, we focused on measuring the induced thermal lens, investigated if it is stable over time and if optical aging or gray-tracking lead to significant changes in the induced lens. This could be a relevant information for space applications. Determining the value $\Delta\tau_{mag}$ was considered to be an ideal candidate, because it is proportional to the absorption coefficients and to the induced thermal lens.

A general drawback of the presented method is, that the thermal lens the HeNe laser experiences, might not be the same, the IR laser or the generated harmonics experience. First of all, the refractive indices and their changes are dependent on the wavelength and polarization in a birefringent crystal. Since the HeNe laser's polarization was not adjusted to match the harmonic's polarization, the thermal lens might not be the same. Second, the HeNe laser experiences the thermal lens integrated over the whole crystal length. In contrast to this, the harmonic is generated over the crystal length. Therefore, it experiences only a part of the induced lens. When information on the absolute value of the thermal lens and its formation is of interest, the wavefront of the generated harmonic needs to be observed. Since our indirect method allowed a stable measurement independent

---

[1]During longterm operation of optical components exposed to high pulse energies, the laser induced damage threshold, especially of the coated surfaces, decreases. This can lead to a dramatic degradation of the optics [30]

from the conversion efficiency and secondly, no wavefront sensors in the ultraviolet were available at the facility, the decision was taken to measure the lens indirect. The experimental realization is explained in the following.

HeNe laser and beamline

As mentioned before, the wavefront deformation was measured on a HeNe laser co-aligned with the IR laser beam. A frequency stabilized cw-HeNe laser with a maximum power of 1 mW was used for the experiments. To ensure a plane wavefront, a spatial filter was introduced in the beamline. It consists of a strong focusing lens ($f = 16.5$ mm) and a pinhole (25 μm) in the focal plane. Because of diffraction, only a monochromatic wave with a plane wavefront shows a single spot in the focal plane, else the spot is surrounded by concentric rings. By placing a pinhole in the focal plane, these impurities can be filtered. That is why the beam shows a Gaussian profile with a defined wave-front after passing the spatial filter [31].

Using a second lens afterward, the $1/e^2$-radius of the beam profile was adjusted to match the IR laser beam profile at 3.2±0.2 mm. The HeNe laser's direction through the crystal was opposite to that of the IR laser. Hereby, an accidental damage of the wavefront sensor due to the high power IR laser or its generated harmonics was prevented. It was coupled into the beamline of the IR laser through the backside of a mirror high-reflective coated for wavelengths at 355, 532 and 1064 nm and leaves it by passing a mirror, coated high-reflective only for 1064 nm. To ensure that the two beams are co-aligned over the crystal length, pinholes in front and behind the crystal were introduced into the beamline.

Shack-Hartmann wavefront detector

The thermal lens formed within the nonlinear crystal was detected by measuring the resulting wavefront deformation with a Shack-Hartmann sensor. Wavefront measurements with Shack-Hartmann sensors find wide application, ranging from adaptive optics in astronomy and high power laser systems to aberration measurements of the cornea in ophthalmology [35]. Such a sensor consists of a micro-lens array and a 2-dimensional detector (here a CCD) in the focal plane of the lenses,
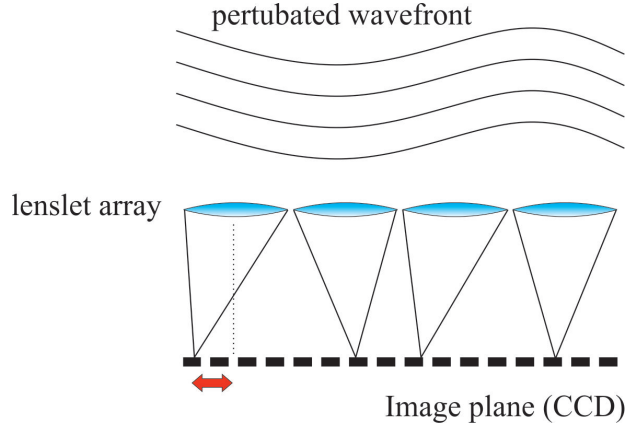
Figure 4.5: Basic principle of a Shack-Hartmann sensor: the local wavefront slope causes a tilt of the focal spot for each lens, which is then detected with e.g. a CCD in the image plane.

its basic principle is depicted in Figure 4.5. The local slope of a distorted wavefront causes an individual tilt of the focal spot for each lens of the lenslet array. The combination of the tilts of different lenses (the local slopes) allows to conclude on the wavefront deformation [25].

For our experiments, a wavefront sensor by Imagine optic Inc. (HASO-3 32), consisting of a lenslet array with $32{\times}40$ lenses with diameters of d $= 160$ μm, was used. Its design allows to determine wavefront deformations with a maximum precision of $\lambda/100$ rms. The resulting precision for the HeNe laser, used for the wavefront measurements, is 6.23 nm rms. However, since the Shack-Hartmann sensor utilized in our experiment was not calibrated for 633 nm, but for 800-1100 nm, the realized precision will be less. To avoid that the measurement is disturbed by background light of the IR laser or its harmonics, the sensor was triggered to the laser with a delay of 200 μs. The maximum acquisition frequency of the Haso-3 32 is 50 Hz. Since wavefront measurements were averaged over 20 images to account for the measurement uncertainties, acquisition frequency was down to 2-3 Hz.

To process and analyze the acquired wavefronts, the original HASO software directly from the supplier was used. For the integration of the local slopes two established possibilities exist. The modal reconstruction, which projects the phase on a polynomial base or the zonal reconstruction, which reconstructs the wavefront by integration of the local derivatives of the wavefront [47]. In this work

the zonal reconstruction was chosen, because it can best determine the low spatial frequencies (as tilt, radius of curvature, third order aberrations). It also allows the reconstruction of the wavefront in polynomial coefficients (e.g. Zernike for circular pupils, Legendre for square pupils). Since we were interested in these low spatial frequencies describing the thermal lensing, the modal reconstruction for a circular wavefront was chosen in the experiment [20].

Modal reconstruction in Zernike polynomials

Zernike polynomials are a sequence of orthogonal polynomials on the unit disk which are often used in adaptive optics to reconstruct wavefronts. They consist of a radial polynomial $R_n^l(\rho)$ and an azimuthal function $e^{il\theta}$, whereby the first radial polynomials can be identified with the classical aberrations as piston, tilt, defocus, astigmatism, coma, trefoil and third-order spherical aberrations (see Figure 4.6) [17]. Especially the defocus term:

$$R_2^0(\rho) = 2\rho^2 - 1 \tag{4.9}$$

was of interest to calculate and monitor $\Delta\tau_{\mathrm{mag}}$ over time. Since the thermal distribution (Eq. 4.7) and hence the thermal lens was expected to be parabolic as well. As it was found out in the experiments, the coefficients of the higher order spherical aberrations (see for example Fig. 4.6i) were usually by two orders smaller than the coefficient of the defocus term.

4.1.6 Third harmonic generation

Third harmonics were generated through two steps with second harmonic generation in a first crystal and sum frequency generation in a second crystal. Both crystals used in the experiment were BiBO crystals cut for type-I phase matching. Radiation at 1064 nm leaves the first crystal therefore s-polarized and the generated radiation at 532 nm leaves it perpendicular to the IR light as f-polarized. For sum frequency generation at type-I phase matching in the second crystal, both needed to be s-polarized. Consequently, a dual-wave plate being a half-wave plate at one of the wavelengths (1064 nm) and a wave-plate at the second wavelength

(a) piston   (b) tilt x   (c) tilt y

(d) defocus   (e) astigmatism 0°   (f) astigmatism 45°

(g) coma x   (h) coma y   (i) spherical aberration ρ^4
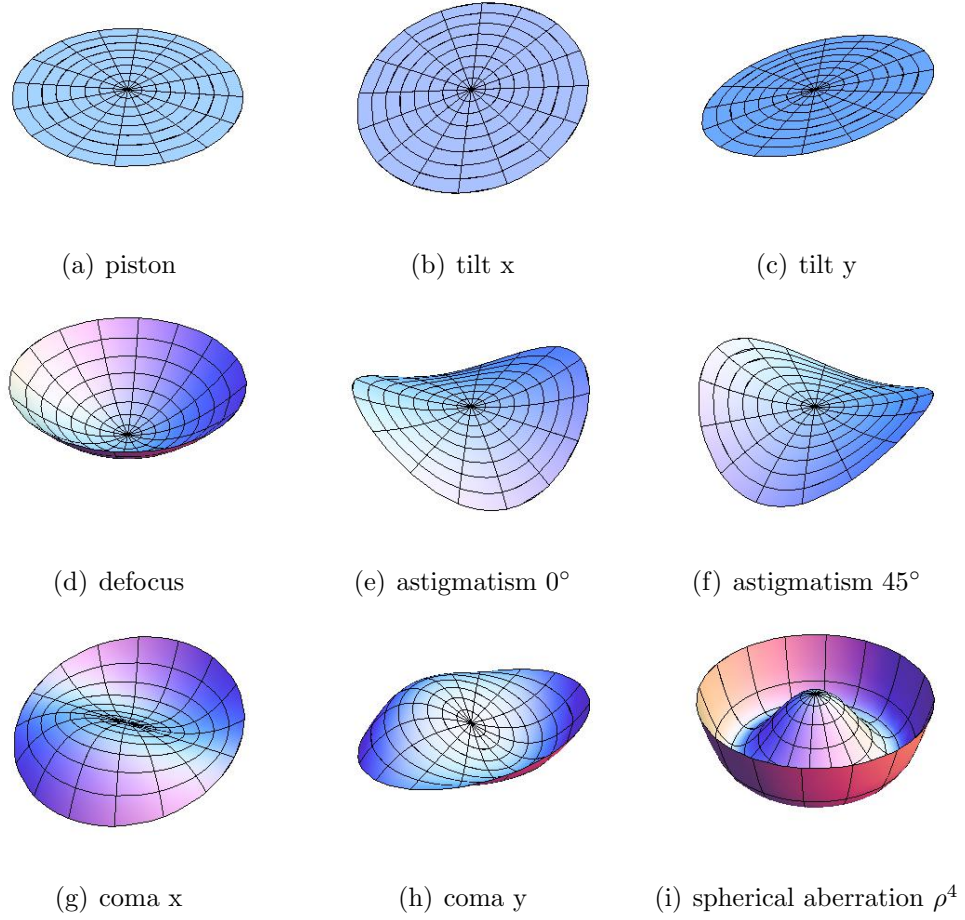
Figure 4.6: First nine Zernike polynomials; of special interest was the defocus term with its parabolic shape. Higher order wavefront deformations were by one to two orders smaller during the SHG and THG measurements.

(532 nm) was introduced in the beamline between the two crystals. By adjusting its orientation, the phasematching conditions can be fulfilled. To measure the conversion efficiency, two additional beam samplers (HR355/HT532+1064) were introduced into the beamline, separating the UV radiation from the fundamental and the second harmonic laser radiation (see figure 5.1).

In dependence of the distance between the two crystals, the walk-off of the generated harmonic leads to a decreased conversion efficiency in the second crystal. For that reason, the distance between the two crystals had to be minimized. Due to
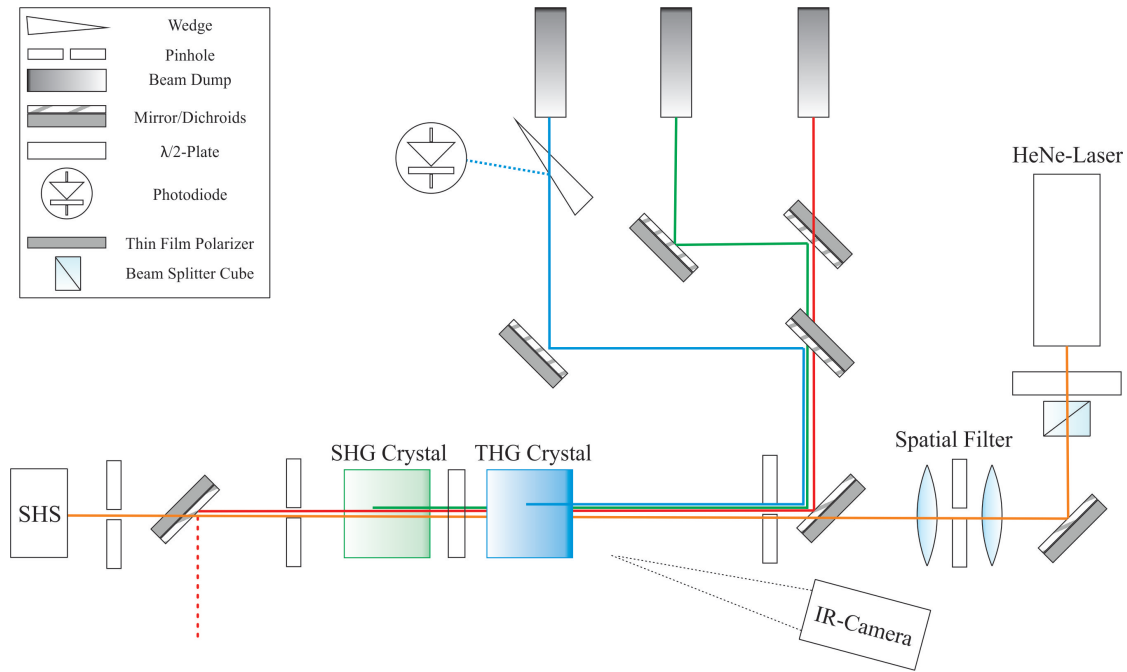
Figure 4.7: Experimental set-up for THG measurements, beamline before the crys-
tals as in Fig. 4.1, the measured wavefront deformation is now caused
by thermal lensing in the SHG crystal as well as in the THG crystal.

the mount design and the half-wave plate in between the crystals, the minimum
possible distance was 8.0±0.2 cm. This short distance between the two crystals,
did not allow us to determine the wavefront distortion caused by the second crystal
isolated. Instead, the wavefront deformations caused by the propagation through
both crystals was measured with the Shack-Hartmann sensor.

4.1.7 Long term operation

The planned operational time of the ADM-Aeolus mission is 3 years or respectively
7 billion laser pulses (at repetition rate of 80 Hz and continuous operation). Thus,
a stable operation of the frequency converting unit must be guaranteed over this
lifetime. That is why long term experiments were carried out within this Diploma
thesis. Since the investigation of frequency conversion over an operational time of
3 years was not feasible, decision was taken to simulate 1 % of the lifetime. Re-
sulting in an exposition of the crystals to 70 million laser pulses. Using our 100 Hz

Infinity laser system, such a longterm experiment was possible in the reasonable time of one week.

It was to investigate, if frequency conversion efficiency and temperature control of the mount are stable, when exposed to ambient temperature changes and during long term operation. Of special interest was the development of the induced thermal lens over time. As mentioned before, KTP crystals show gray-tracking during longterm operation. This leads to stronger absorption and a change in the focal length of the induced thermal lens. Other processes that could take place during long term operation are optical aging or the occurrence of damage. A thermal lens itself might not be a problem for the mission, since the optics (lenses in the beamline) will be adjusted to guarantee a collimated beam before the satellite is packed onto a rocket. However, if the thermal lens is not stable during the operation in space, the optics on the satellite can not be readjusted anymore.

4.2 Results

The results of the second harmonic and third harmonic generation experiments are presented in the following. Furthermore, the results obtained during longterm operation of the frequency conversion unit are given. The final discussion of the presented results is found in chapter 7.

4.2.1 Qualification of the mount design

In order to test, if the mount design meets the requirements as low power consumption and stable homogenous heating of the crystals, we started by doing thermal steady state simulations with the finite element program by Ansys Inc.. Simulation showed a homogeneous heating of the crystal holder with variations of less than 40 mK (see Figure 4.8). The Macor baseplate demonstrated to be an excellent isolator with its low thermal conductivity (1.46 W/(mK) [41]). Power consumption for the operation at 30°C within an atmosphere of 22°C was calculated to be 0.6 W, whereby only 0.165 W were losses due to the contact of the crystal holder with the Macor plate.

Experimentally, the power consumption to heat the crystal to 30°C was measured to be 0.42 W. Hence, measured power consumption was in good agreement with the simulation.

Heating and temperature control was done with a PID controller and two 9.6 Ω resistive heaters. The controller operates by switching a circuit on/off electronically at optimized parameters. Consequently, the voltage on this relay circuit had to be chosen to match the power consumption. Two supplies for the relay circuit were available, a 3 V or a 24 V power supply. For heating the crystal to a phase matching temperature of 30°C, the 3 V power supply was chosen. With the two resistive heaters switched in series, a maximum power of 0.46 W at a 100 % duty cycle results, matching the requirements perfectly. In Figure 4.9, the duty cycle of the heaters is shown on the left and the crystal's temperature variations over time on the right. Depicted is the crystal's surface temperature over time, measured with the IR camera. One sees fast oscillations with an amplitude of 50 mK due to the measurement accuracy of the IR camera, and slower variations

(a) baseplate
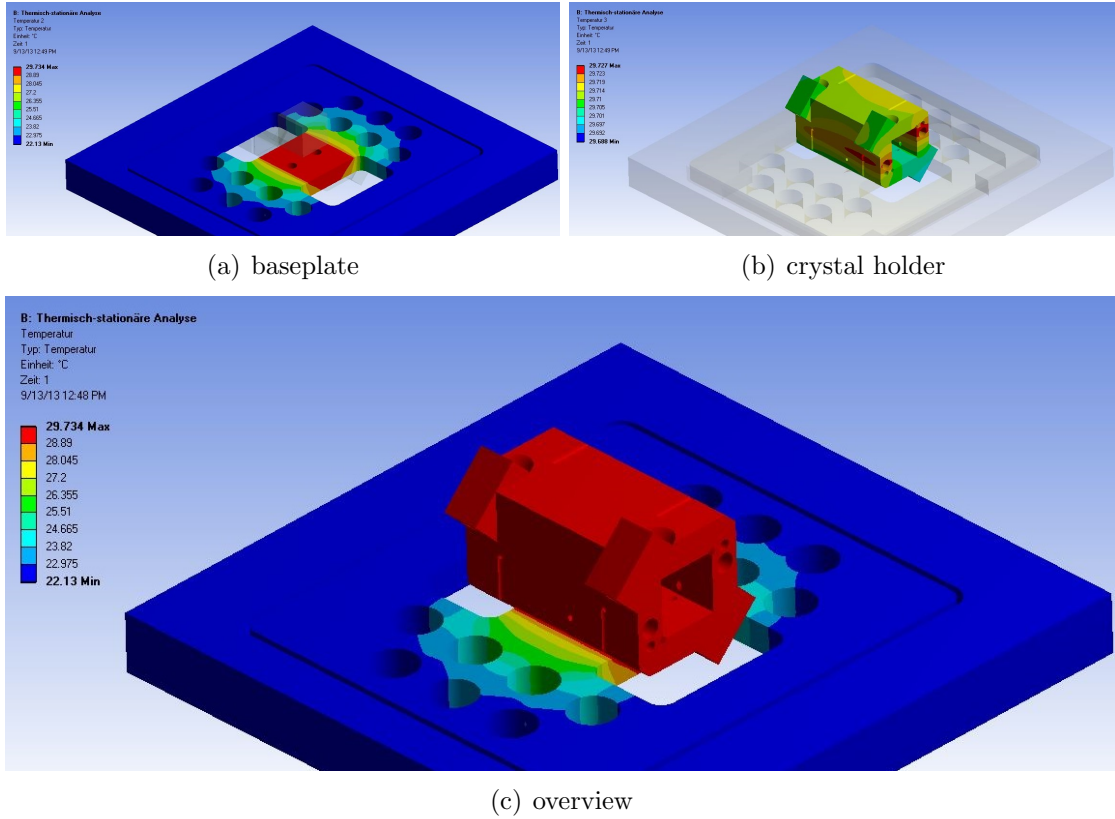

(b) crystal holder

(c) overview

Figure 4.8: Thermal steady-state simulation of the crystal holder mounted on the baseplate and heated with a heat flux of 0.6 W into the drill holes (c). The low thermal conductive baseplate ensures low thermal losses of 0.165 W (a). The temperature of the crystal holder was found to be homogenous within an accuracy of 40 mK (b). Simulated with Ansys.
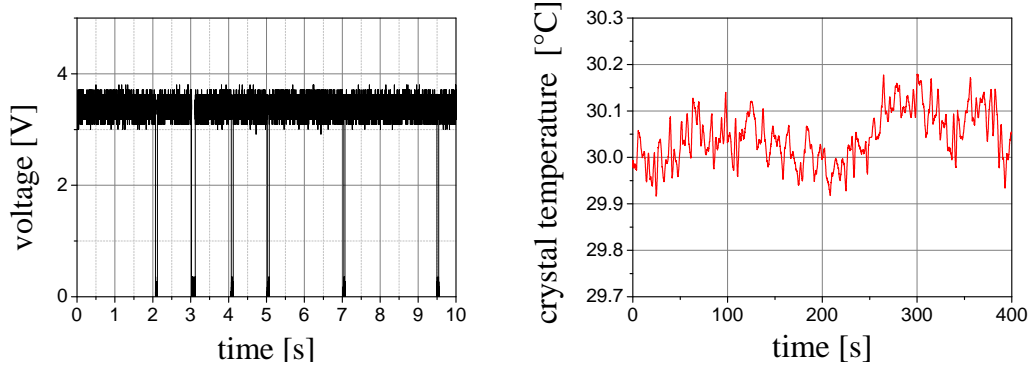
Figure 4.9: Voltage on the resistive heaters showing the almost 100 % duty cycle (left) and temperature on the crystal surface over time measured with the IR-camera. The fast oscillations of 50 mK are due to the accuracy of the camera, the slow variations show the accuracy of the temperature control.

with an amplitude of 0.1 K describing the accuracy of the temperature control. Since the BiBO crystals were cut for phase matching at 56.8°C, a stable operation at this temperature was needed as well. Here, power consumption was measured to be 2.17 W. In consequence, the relay circuits power supply with 24 V needed to be chosen, with the resistive heaters connected in series as well, resulting in a maximum power of 30 W. Hence, duty time was down to 7 %. However, stable operation with variations of less than 0.1 K were measured with the IR camera. Next, the spatial homogeneity of the crystal's temperature was controlled with the IR camera. It was found to vary less than 0.1 K over the crystals' front facet. Hence, homogeneity of the crystals heating was measured to be ±0.1 K in space and time. As listed in table 3.1, the most demanding situation in our experiments is found for third harmonic generation with a 10 mm long BiBO crystal, having a FWHM temperature bandwidth of only 0.9 K. The temperature control's accuracy therefore ensures a stable conversion efficiency with variations of less than 3.5 % (when underlying a sinc^2-dependency of the conversion efficiency on the temperature at sum frequency generation with BiBO crystals, see also figure 2.3).
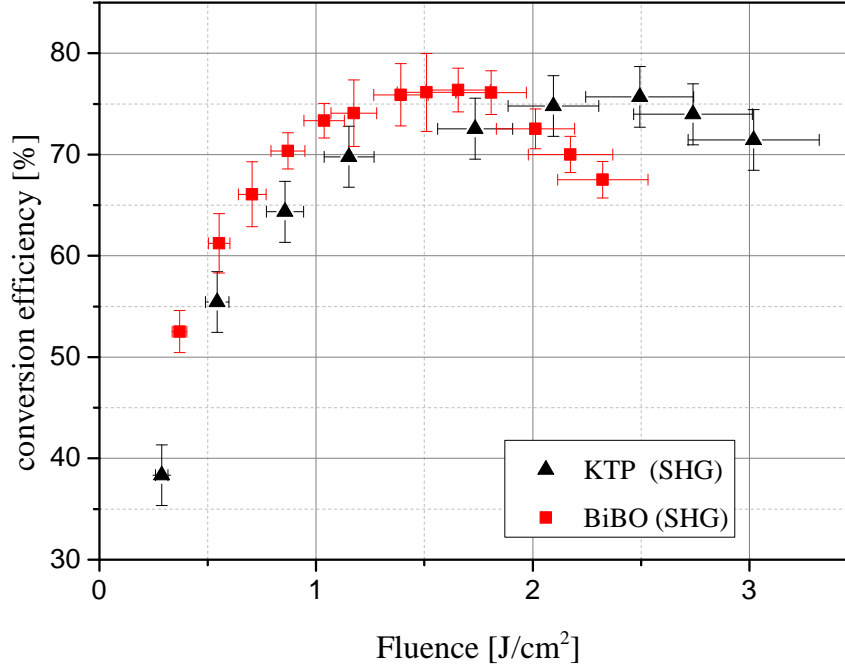
Figure 4.10: Measured conversion efficiencies for BiBO and KTP crystals at second harmonic generation, both crystals show high maximum conversion efficiencies of 76±3 %, for the BiBO crystal the maximum is reached already at lower fluences than for the KTP crystal (1.66 ± 0.15 J/cm^2 vs. 2.50 ± 0.25 J/cm^2).

4.2.2 Second harmonic generation

Efficiency at second harmonic generation versus fluence on the crystals' entrance facets for KTP and BiBO crystals are shown in figure 4.10. The maximum conversion efficiency was realized for the KTP crystal at a fluence of 2.50 ± 0.25 J/cm^2 with an efficiency of 76±3 %. Pulse energy of the infrared laser was here 58 mJ, the resulting pulse energy of the second harmonic was measured to be 44 mJ. For the BiBO crystal, the conversion efficiency was in the same range with a maximum of also 76±3 %, however the maximum is found at lower fluences (1.66 ± 0.15 J/cm^2). The pulse energy of the second harmonic at maximum conversion efficiency was 40 mJ at a pulse energy of the fundamental wave of 54 mJ.

As can be seen, pulse energies at maximum conversion efficiency are in the same range in KTP and in BiBO crystals, although measured at different fluences. This is due to the fact, that the telescope was adjusted in between the two measurements. The $1/e^2$-beamwidth was wider for the measurements with BiBO (3.16×2.60 mm^2) than for KTP (2.90×2.42 mm^2). The adjustment was done to take into account the lower damage threshold of BiBO crystals compared to KTP crystals (see table 3.1). In both experiments, the beam was collimated with divergencies (full angles) of 0.2 mrad for measurements with BiBO crystals and 9.4 mrad for the measurements with KTP crystals.

Thermal lensing and temperature on the exit facets

Without phase-matching but the IR laser turned on, both crystals showed now self-heating and no relevant wavefront deformation was measured with the Shack-Hartmann sensor. But with the phase-matching fulfilled, differences could be found between BiBO and KTP crystals due to the different absorption at the generated second harmonic.

Relevant heating of the crystal's exit facet was found for the KTP crystal, whereas no temperature changes were found on the exit facet of the BiBO crystal. The 2-dimensional temperature distributions on the exit facets during second harmonic generation are shown in Figure 4.11, for the KTP crystal a Gaussian like temperature distribution with a maximum amplitude of $+5.0\pm0.2$ °C was found, whereas the temperature is homogenous on the BiBO crystal's exit facet (±0.1 °C).

The same applies for the measured wavefront deformation (see Figure 4.12). No relevant thermal lensing was measured for the BiBO crystal with a defocus term of 3.3 ± 2.6 nm and a $\Delta\tau_{\mathrm{mag}}$ of 6.6 ± 5.3 nm, which is just the measurement accuracy of the SHS. Whereas a significant wavefront deformation was found in the KTP crystal, with a coefficient of the defocus term of 81 ± 2 nm and a $\Delta\tau_{\mathrm{mag}}$ of 163 ± 5 nm. The thermal lens had a focus length of 12 ± 2 m, whereby we need to remind that the lens the HeNe laser experiences might not be identical to the lens the generated harmonic experiences.
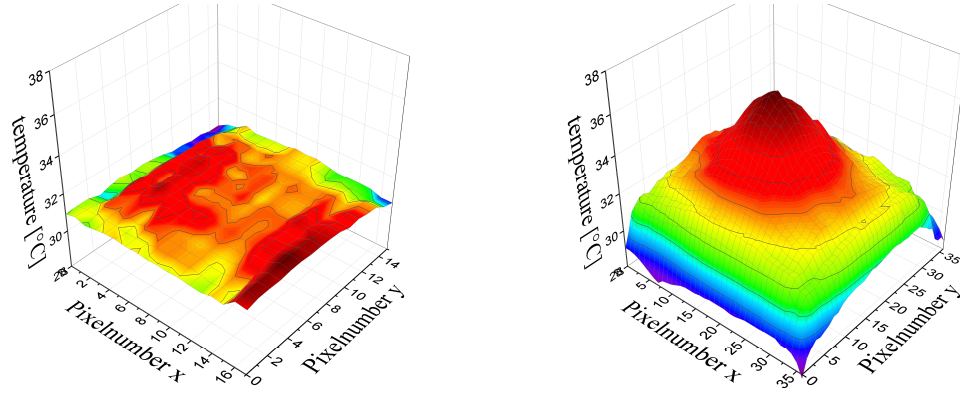
Figure 4.11: Infrared images of the crystals' surfaces during second harmonic generation (BiBO crystal on the left, KTP crystal on the right), no relevant heating occurs in the BiBO crystal, whereas the temperature increases with a Gaussian like shape and an amplitude of 5.0±0.2 °C on the exit facet of the KTP crystal.
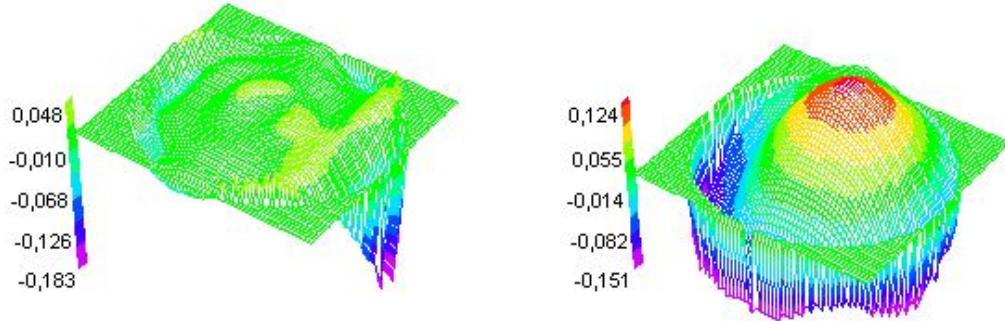

Figure 4.12: Wavefronts during second harmonic generation (BiBO crystal on the left, KTP crystal on the right), in contrast to the KTP crystal no relevant wavefront deformation occurs in the BiBO crystal.
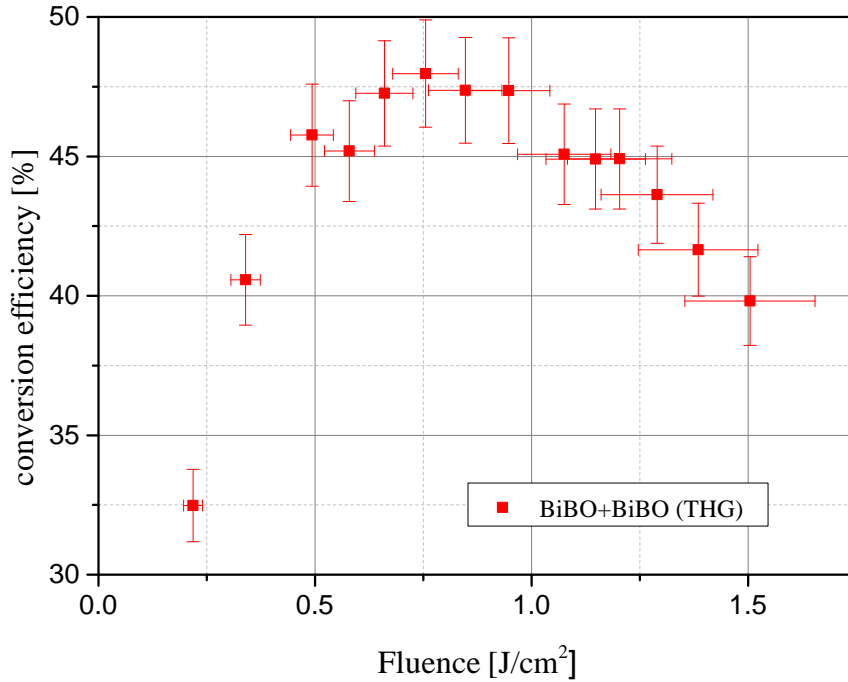
Figure 4.13: Conversion efficiencies versus fluences for a combination of two BiBO crystals at second harmonic generation plus sum frequency generation. A maximum conversion efficiency of 48±2 % was realized.

4.2.3 Third harmonic generation

Conversion efficiency at third harmonic generation was evaluated for a combination of two BiBO crystals (10.4 mm and 10 mm), both cut for type-I phasematching. The beamprofile on the entrance facet of the first crystal and the beam's divergence were the same as in the SHG experiments for BiBO crystals.

In Figure 4.13 the conversion efficiency versus fluence is depicted. The apparent maximum was reached at a fluence of 0.75±0.08 J/cm² with an efficiency as high as 48±2 %. Pulse energy in the ultraviolet was measured to be 13 mJ at maximum conversion efficiency with a pulse energy of 27 mJ of the fundamental laser. The conversion efficiency is strongly dependent on the fluence and already decreases by 20 %, when fluence is increased by 0.7 J/cm² above the optimum. Also, the maximum conversion efficiency for THG is reached at a lower fluence than at SHG.

This is explained by the fact, that one photon at the fundamental and one photon at the second harmonic are needed to interact through the nonlinear polarization at SFG. Hence, if walk-off is not significantly influencing the SFG, the optimum should be found at a conversion efficiency of 66 % for the second harmonic. In that case, the number of photons at the fundamental wavelength is equal to that at the second harmonic. And indeed, the optimum for the THG unit is found at this corresponding fluence (compare also with SHG efficiencies in Figure 4.10).

Thermal lensing and temperature on the exit facet:

The HeNe laser passes two crystals and the half-wave plate. Therefore, the measured wavefront deformation is a result of the propagation through these three optical elements. But wavefront deformation due to second harmonic generation can be neglected for BiBO crystals (as it was shown in section 4.2.2) and the half-wave plate was found to be of no impact as well. Therefore, the measured wavefront deformation can be attributed to the absorption at the third harmonic in the BiBO crystal. As an indicator for a higher absorption coefficient at a wavelength of 355 nm than at 532 nm or 1064 nm in BiBO crystals, a wavefront deformation was now observed. The defocus term was found to be 40±8 nm, respectively a $\Delta\tau_{\mathrm{mag}}$ of 79±16 nm. Also, on the exit facet of the second crystal, a temperature gradient with an amplitude of 0.9±0.1 K was detected with the IR camera.
When comparing with the experiments at second harmonic generation, the discovered self-heating and lensing at third harmonic generation in the two BiBO crystals is smaller than in KTP crystals at second harmonic generation.

4.2.4 Longterm operation

Of special interest for the application in space, is the stability of the conversion efficiency and thermal lensing over the long operational time of three years. For the KTP crystal, a longterm test at SHG and for the BiBO crystal, longterm tests at SHG and at SHG+SFG were therefore carried out.
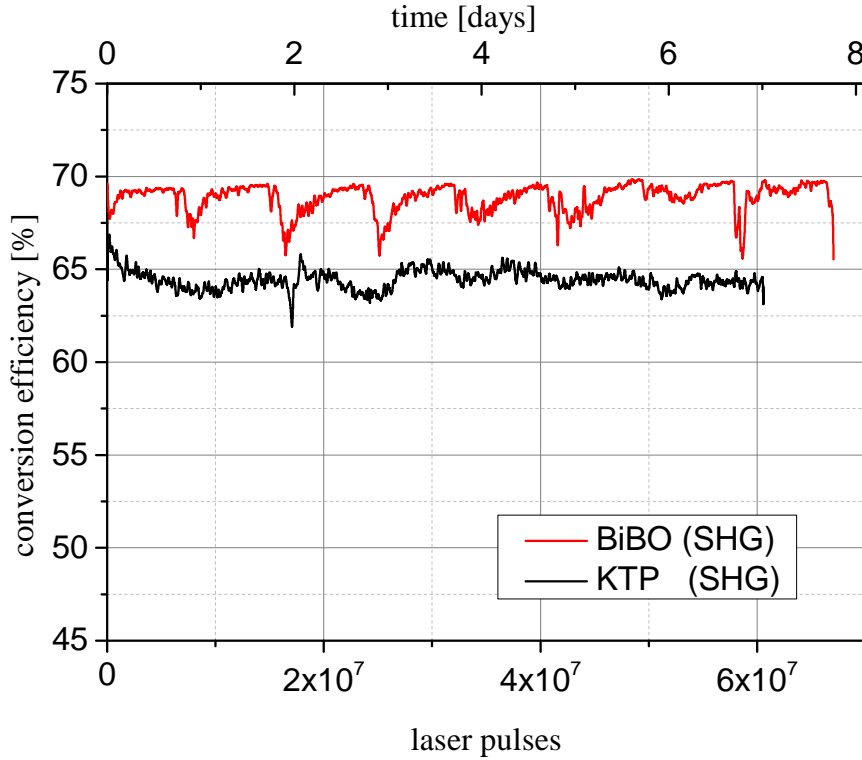
Figure 4.14: Stable frequency conversion efficiencies were measured for BiBO crystal and KTP crystal at second harmonic generation during long term operation over approx. 1 % of the ADM-Aeolus mission's lifetime. The significant drops of 4±1 % every 24 hours for the BiBO crystal were due to an inaccurate temperature control. The systematically decreasing conversion efficiency over the first 24 hours in the KTP crystal could be due to the gray-tracking, however it is not significant.

Second harmonic generation

The experiments were performed over more than 6×10^7 laser pulses or respectively more than 7 days at a repetition rate of 100 Hz, which simulates approximately 1 % of the operational time of the ADM-Aeolus mission. The investigation was performed at pulse energies of 52±2 mJ and fluences of 1.6±0.2 J/cm^2 for the BiBO crystal and at pulse energies of 77±4 mJ and fluences of 2.4±0.3 J/cm^2 for the KTP crystal. In Figure 4.14, the realized conversion efficiency during longterm operation is depicted for the KTP crystal and the BiBO crystal.

The conversion efficiency for the BiBO crystal was 69±1 % and did not show any systematic decline over time. However, significant drops of 4±1 % were found every 24 hours. They are due to a failure of the PID-controller, probably caused by a wrong temperature measurement when the controller was exposed to direct sunlight. Therefore, the observed drops in conversion efficiency are not caused by processes within the BiBO crystal or its small temperature acceptance bandwidth. During the experiment with the KTP crystal, the conversion efficiency decreased over the first 1×10^6 pulses systematically from 67 % to 63 %. Thereafter, it stabilized at 64±1 % (see Figure 4.14).

Wavefront deformation and self-heating during longterm operation at SHG

The temperature distribution on the exit facets of both crystals showed no tendencies or significant variations over time. For the KTP crystal, the temperature difference between the crystal's center and the crystal's contact area with the mount was stable at 5.0±1.0 °C, in the BiBO crystal it was 0.0±0.3 °C. See also Figure 4.11 for the temperature distributions.

In contrast, the optical path length difference $\Delta\tau_{\mathrm{mag}}$ increased over time at the KTP crystal. It started at 160±5 nm and asymptotically reached 193±4 nm, showing an exponential development with a half-life time of 1.1×10^7 laser shots. The curve is depicted in Figure 4.15 with an exponential fit to it. Also in the literature, this exponential development over time is described for the gray-tracking. It saturates when the maximum possible number of color centers has formed [4]. The observed development is therefore suspected to be caused by gray-tracking. Following the development of $\Delta\tau_{\mathrm{mag}}$, the thermal lens changed from a focal length of 12±2 m to a focal length of 8±2 m during long term operation, thus focusing of the beam increased over time.

As Boulanger et al. [4] showed, absorption centers anneal when the crystal is exposed to high temperatures above 120 °C. The KTP crystal was therefore heated to 125 °C over 24 hours and the measurement of the thermal lens $\Delta\tau_{\mathrm{mag}}$ was repeated afterwards. It was found to return to the initial value at 155±7 nm. Which indicates once more that the change was due to gray-tracking. In the BiBO crystal, $\Delta\tau_{\mathrm{mag}}$ was found to be (within measurement accuracy) stable over the longterm
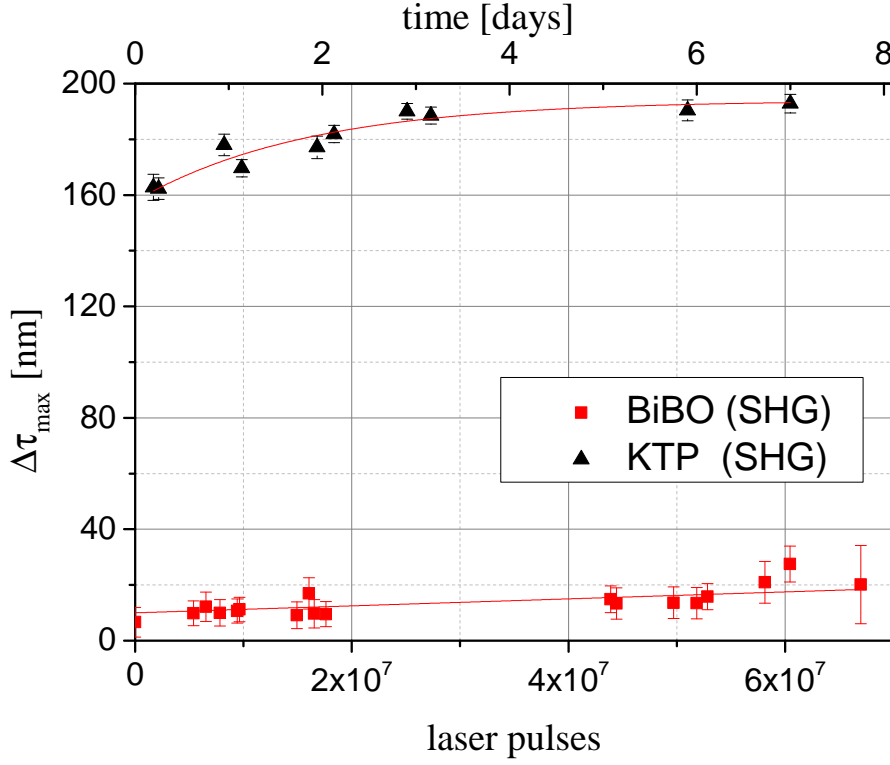
Figure 4.15: Evolution of $\Delta\tau_{\mathrm{mag}}$ over time during longterm operation at second harmonic generation in KTP and BiBO crystals. A significant increase with an exponential saturation is found in the KTP crystal, whereas it is stable in the BiBO crystal.

operation at 15±5 nm, indicating that no changes in absorption occurred in the crystal bulk.

Third harmonic generation

To be comparable with the studies at second harmonic generation, the longterm operation at third harmonic generation was carried out at pulse energies of 55±3 mJ and fluences of 1.4±0.2 J/cm² in the infrared. Conversion efficiency was 35±2 % with pulse energies of the generated radiation at 355 nm of 20±1.3 mJ. We observed no systematic decrease in conversion efficiency during the operational time of 160 hours (see Figure 4.16). The wavefront deformation and hence $\Delta\tau_{\mathrm{mag}}$ stabilized after rising fast at 120±20 nm (Fig. 4.17). The rising at the start of the

Figure 4.16: Conversion efficiency at third harmonic generation over time and laser pulses for a combination of two BiBO crystals, no significant decrease in conversion efficiency was detected during long term operation.
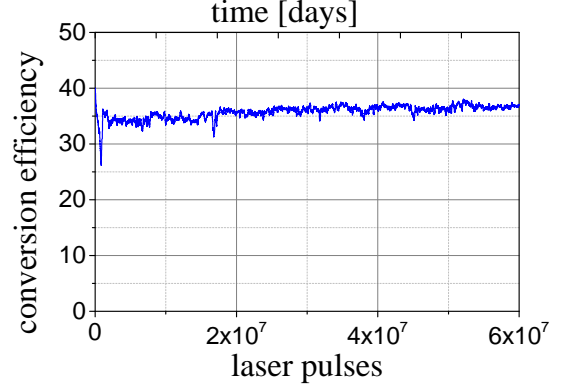
Figure 4.17: $\Delta\tau_{max}$ over time during longterm operation at third harmonic generation with BiBO+BiBO. After rising fast during the first shots, it stabilizes at 120 ± 20 nm.
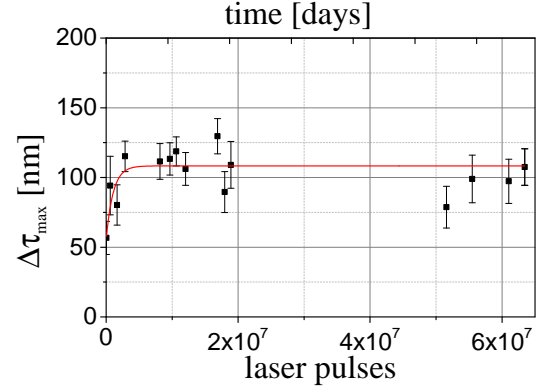
experiment (during the first 0.5×10^6 pulses) may represent the stabilization of the thermal lens. An influence on the conversion efficiency was not detected. As already observed at the longterm experiments for second harmonic generation, the temperature distribution on the exit facet was constant over time showing a Gaussian like distribution with an amplitude of $+1\pm0.3$ °C.

5 Laser calorimetric absorption measurements

Absolute measurements of the absorption coefficients can not be carried out during the frequency conversion experiments with the Shack-Hartmann sensor (as described in Section 4.1.5). Still, the absolute value of the absorption coefficient is an important property of the nonlinear crystal and describes its optical quality. For this reason, laser calorimetric absorption measurements were carried out. An already existing set-up at the Institute of Technical Physics (DLR) was used for this study. In the first section, the measurement principle is explained, in the second, the properties of the used set-up and the investigated crystals are given. Afterwards, the measured absorption coefficients are presented.

5.1 Metrology of the absorption coefficient

Measuring low absorption coefficients in the range of parts per million per centimeter (ppm/cm) is a demanding task, since simple measurements of the transmissivity are not accurate enough [27]. Therefore, effort was spent in the past few decades to develop accurate techniques. Fundamental works on laser calorimetry were carried out by Hass et al. in 1978 for example [18]. The International Organization for Standardization published the ISO 11551 norm in 1997, wherein laser calorimetry was chosen as the standard method to determine the absorption of optical laser components [51]. In the following, the basic principle of the ISO 11551 test procedure is presented.

A thermally isolated probe (here the nonlinear crystal) is irradiated with a laser

beam of a specific power P. In dependence of the absorption coefficient, this leads to a heating of the probe. The underlying model assumes that the radiative losses are linear, that the temperature of the probe is homogenous at all times and that the probe is in thermal equilibrium prior to the experiment. The temperature development is then described by [51]:

$$\frac{d}{dt}\Delta T = \frac{\alpha LP}{mc_{\mathrm{p}}} - \gamma \Delta T \tag{5.1}$$

where ΔT describes the change in temperature of the irradiated probe, L is the probe's length, α is the absorption coefficient, m is the probe's mass and c_{p} is its specific heat capacity. The linear term with the coefficient γ describes losses due to heat radiation and conduction. The laser is turned on at time t_0, and turned off at a time t_1. From Equation 5.1 one obtains the following temperature development:

$$
\begin{aligned}
\Delta T &= 0 & &\text{for } t < t_0 \text{ (thermal equilibrium)} \\
&= \frac{\alpha LP}{mc_{\mathrm{p}}}\left(1 - e^{-\gamma(t-t_0)}\right) & &\text{for } t_0 < t < t_1 \text{ (laser on, heating)} \\
&= \frac{\alpha LP}{mc_{\mathrm{p}}}\left(e^{-\gamma(t-t_1)} - e^{-\gamma(t-t_0)}\right) & &\text{for } t > t_1 \text{ (laser off, cooling)}
\end{aligned}
\tag{5.2}
$$

For known values of the heat capacity, mass and laser power, the absorption coefficient can be derived from the probe's temperature over time. Mainly two different methods to determine the absorption coefficient from the temperature are described in the literature: the gradient method [27] for small laser powers and the pulse method [51]. In this work, the absorption coefficient was determined with the second method following the ISO norm 11551 [21].

Hereby, an exponential curve of the type $f(t) = A + B\exp(-\gamma t)$ is fitted to the recorded data during the cooling of the probe ($t > t_1$). The temperature is then extrapolated to the temperature ΔT_{P} at a time $t_p = (t_0 + t_1)/2$:

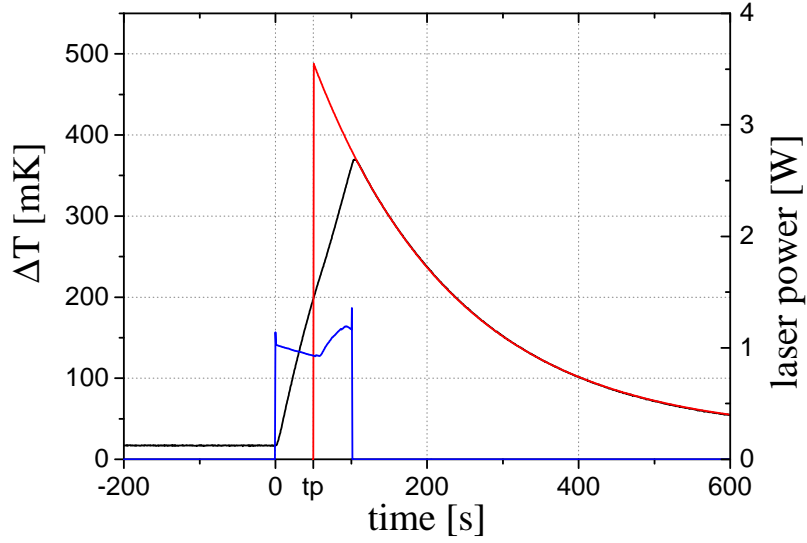$$\Delta T_{\mathrm{P}} = A + B\exp\left(-\gamma \frac{t_0 + t_1}{2}\right) \tag{5.3}$$

Figure 5.1: Temperature over time during laser calorimetry (black line), the laser power is depicted in blue. Exemplarily, the obtained curve for a KTP crystal after longterm operation is depicted. In the pulse method, an exponential fit is applied to the data during cooling (red line) and an extrapolated temperature at time t_p is determined. With Equation 5.5, the absorption coefficient is then calculated.

whereby A, B and γ are derived from the fit. Substituting Equation 5.3 in Equation 5.2 yields to:

$$\alpha = \frac{\Delta T_P m c_p}{L P t_b} \cdot 0.5 \gamma t_b / \sinh(\gamma t_b/2) \tag{5.4}$$

for the absorption coefficient. Here $t_b = t_1 - t_0$ is defined to be the total duration of the irradiation. Since radiative losses are small at ambient temperature $\gamma t_b < 0.5$, the term $0.5 \gamma t_b / \sinh(\gamma t_b/2)$ can simply be approximated by one [21], yielding to a simple expression for the absorption coefficient:

$$\alpha = \frac{\Delta T_P m c_p}{L P t_b} \tag{5.5}$$

5.2 Experimental set-up

A cw-laser at a power of up to 15-20 W, a beam width of maximal 6 mm and a wavelength of 940 nm at an unknown polarization was used for the laser calorimetry. The detection limit of the set-up is as low as 5 ppm/cm, measurement uncertainty is in the range of 10 %.

Although an investigation of the absorption coefficients at the fundamental wavelength (1064 nm) or its harmonics (532 and 355 nm) would have been of interest, absorption coefficients at 940 nm already allow for a comparison of the investigated crystals. An investigation at the above stated wavelengths was not possible with the set-up. During the experiment, the crystal's temperature was measured with a thermoelectric resistance attached to the crystal's side facets. The thermal contact was improved by applying a small amount of thermally conductive paste. Apart from this, the probe is thermally isolated and fixed at its position only with low thermal conductive plastic screws. Its temperature is recorded during irradiation with the laser and afterwards for at least 200 seconds.

The investigated crystals were the KTP and BiBO crystals used in the experiments for frequency conversion, as well as thin slices (2.7 mm) of KTP and BiBO crystals and, for comparison, a 19.5 mm long LBO crystal. The physical properties of the crystals as density and specific heat capacity were adopted from Nikogosyan [32, 33].

5.3 Summary of the laser calorimetry

The determined absorption coefficients are listed in table 5.1. For all investigated crystals, they were below 1 %/cm. On the one hand, differences were found between BiBO and LBO crystals with absorption coefficients as low as 40-60 ppm/cm (BiBO) and 84±10 ppm/cm (LBO). On the other hand, KTP crystals showed an absorption coefficient of 810±80 ppm/cm. Gray-tracking was assumed to have occurred in the KTP crystal during the longterm operation (section 4.2.4) and laser calorimetry was therefore repeated after the longterm experiment. It was found to be 8.8×10^3 ppm/cm directly after the longterm test, and decreased to 1.9×10^3 ppm/cm after heating for 24 hours at 125 °C.

Table 5.1: Laser calorimetric measured absorption coefficients α for the investigated nonlinear crystals, KTP shows higher absorption, gray-tracking during longterm operation and annealing when heated. The difference between the BiBO SHG and THG crystal might be due to the different coating transmissivities and absorptions (THG-crystal: AR-coated 355/532/1064 nm, SHG-crystal: AR-coated 532/1064).

Crystal	for	α (ppm/cm)
BiBO	SHG	60
	THG	40
LBO	SHG	84
KTP	SHG (Thin-Slice)	810
	SHG (after longterm test)	8800
	SHG (after heating)	1900

6 Numerical simulation with Commod Pro

In addition to the experimental investigations, numerical simulations of the conducted experiments were carried out. A good prediction of conversion efficiency allows to study the influence of laser parameters on the conversion efficiency separately and systematically in the future. Another advantage of the numerical approach is the opportunity to get to know if all physical processes relevant for the frequency conversion are understood and considered. Besides this, it allows to reduce costs by choosing optimum crystals in the future.

6.1 Numerical simulation

The commercial software *Commod Pro* by Oxalis-Laser allows to numerically evaluate the propagation of coherent light through bulk materials of optical elements and to simulate linear or nonlinear processes. A graphical user interface allows to align the optical elements in an arbitrary combination by simply dragging and dropping the representing icons. The physical properties like the beam profile, crystal data and interacting beams etc. are then entered by the user. After choosing the calculation mode, Commod Pro compiles and executes the numerical diagrams.

Two propagation modes are available in Commod Pro: the optical geometric propagation of parallel beams or Fresnel's propagation. In this work, the latter was chosen to take diffraction effects into account. Mathematically, the propagation of the electrical fields $E_l(x, y, z, t)$ is then described by nonlinear equations, similar
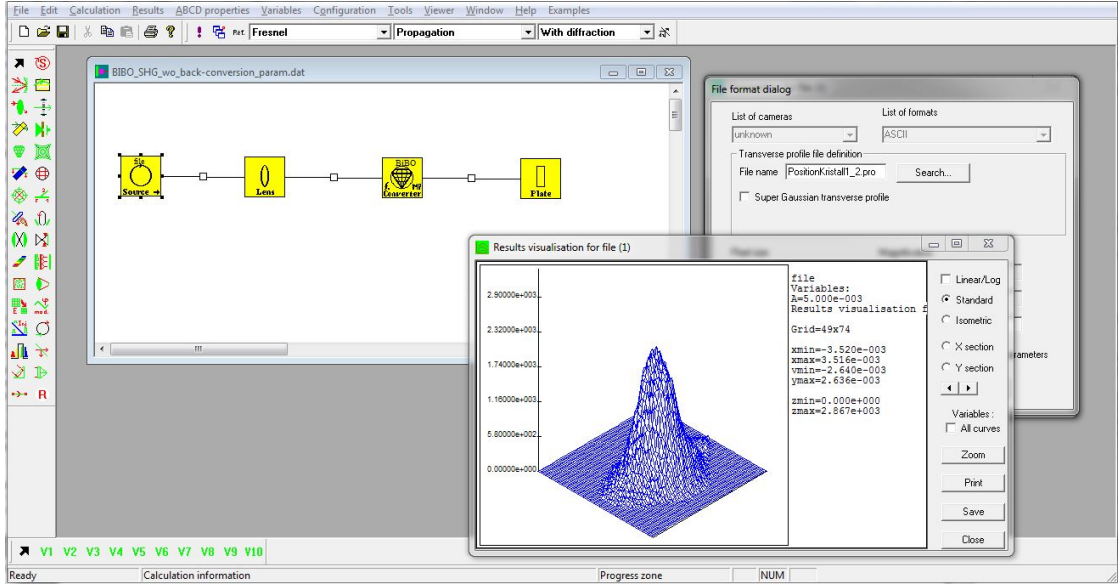
Figure 6.1: Graphical interface of Commod Pro with a simulation configuration for second harmonic generation with BiBO and a displayed beam profile, which was measured with the beam profiler during SHG experiments.

to the Schrödinger equation, coupled with source terms:

$$\left(-2ik_l\left(\frac{\partial}{\partial t} + v_g^l\nabla\right) + \xi_l\Delta + G_l\frac{\partial^2}{\partial t^2}\right)E_l - 2ik_lh_l(x,y,z,E_1,...,E_N) = 0 \quad (6.1)$$

with v_g^l the group velocity, G_l the group velocity dispersion and $h_l(x,y,z,E_1,...,E_N)$ an operator dependent on the interaction with the medium. Of special interest in this work was the interaction of the electric fields through the nonlinear polarization and their propagation through biaxial crystals. The first is done, either through a numerical approach or analytically. The numerical method solves the differential equations (similar to Equation 2.16) with a Runge-Kutta algorithm, the analytical method uses an evaluation of the Jacobi elliptic function (similar to Equation 2.24). Since both methods showed the same results with the analytical method being faster, the analytical method was chosen in this work. The grid size over the crystal length is chosen by Commod Pro, so that the coupling of the electric fields can be calculated separately from the propagation through the crystal. Propagation then takes into account double refraction and diffraction. Since ab-

sorption coefficients for the investigated crystals are small (ppm/cm), absorption was neglected in our simulations. Another dependency neglected in the simulations, is the influence of the wavefront on the conversion efficiency. The possibility to measure and systematically modify the absolute wavefront of the fundamental laser was not given in the conducted experiments.

The optical components needed for the simulations were hence the beam source, a lens to adapt divergence of the beam, the nonlinear crystals and if necessary a half-wave plate (between the crystals at third harmonic generation).

To match the experimental set-up perfectly, an image of the beam profiles on the crystals' entrance facets was taken with a CCD beam profiler and processed for the application in Commod Pro. The temporal profile, measured with a fast photodiode and oscilloscope, was entered as well (see for example Figure 4.2).

Pulse energy and polarization were then entered according to the experimental situations. The divergence or respectively convergence of the beam was measured with the beam profiler as well, measuring the beam diameter at different positions over the beamline. Since measurements were done in the far-field, a linear model was fitted to the obtained data [11]. A focal length was calculated and a corresponding lens was then placed in front of the crystals in the simulations.

The crystal parameters like length and cutting angles (θ, φ) as well as the phase matching temperature were entered. To specify the crystal, the refractive indices in form of Sellmeier equations and their temperature dependencies needed to be given in text-files. Also the dielectric tensor d_{ij} in the crystallooptical coordinates was entered in a text-file. After choosing the type of phasematching (type I or II) and selecting the interacting beams (e.g. s+s=f) and wavelengths, Commod Pro allows to calculate the optimum orientation of the crystal with a maximized value of the effective nonlinearity d_{eff}.

The walk-off was taken into account in the simulations and calculation was done in a 8×8 mm^2 space with a grid of 32×32 calculation points and 30 ns in time, divided into a grid of 32 calculation points. For the KTP crystal, the Sellmeier equation and temperature dependency of the refractive indices were taken from the data sheet of the manufacturer, the dielectric tensor was adopted from Nikogosyan [33]. For the BiBO crystal, the Sellmeier equations and the dielectric tensor were not available directly from the supplier and therefore adopted from Hellwig et al. [19],
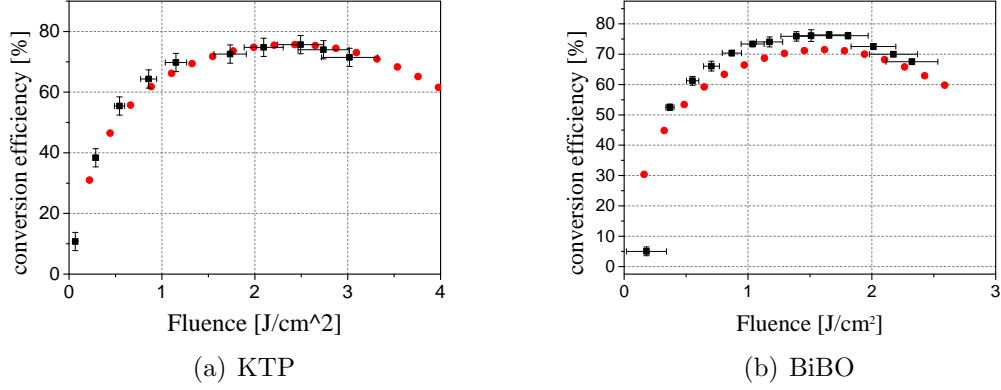
(a) KTP

(b) BiBO

Figure 6.2: Comparison of simulated (red) and measured (black) conversion efficiency at SHG for KTP and BiBO. For both crystals, simulated and measured conversion efficiencies are in good agreement. However, an energy dependent phase-mismatch had to be introduced in the simulation to account for the back conversion at higher fluences (above $2 \ \text{J/cm}^2$ for KTP, above $1.5 \ \text{J/cm}^2$ for BiBO).

the temperature dependencies of the refractive indices were taken from Umemura et al. [48].

6.2 Results

Simulated conversion efficiencies at second harmonic generation for the KTP and BiBO crystals are depicted in figure 6.2. For better comparison, the experimentally realized efficiencies are depicted in the figure as well. At laser fluences under $2 \ \text{J/cm}^2$ for the KTP crystal and under $1.5 \ \text{J/cm}^2$ for the BiBO crystal, conversion efficiency was found to increase continuously with fluence. Here, the experimental results and the simulated frequency conversion matches well one another without any modifications. Per contra, simulated and experimentally realized conversion efficiencies were found to diverge for higher fluences. The conversion efficiency continued to increase with fluence in the simulation whereas it started to decrease in the experiment. Thus, back conversion becomes a dominating effect at higher fluences (or respectively pulse energies) in the experiment. From Equation 2.24

follows, that a process leading to an increasing dephasing δ needs to be present in the experiment. The process leading to that decreasing conversion efficiency at higher pulse energies seems not to be respected within the simulation.

An artificial phase-mismatch of the form $a + x/b$ in dependence of the pulse energy x and two variables a, b was therefore introduced in the simulation. The variables a, b were chosen, by fitting the simulated curve to the experimental data. As to see in Figure 6.2, the simulation is then in line with the experiment. Simulated conversion efficiency and experimental data for both KTP and BiBO crystals then deviate less than 5 % in conversion efficiency for all fluences in between 0.3 J/cm^2 and 3 J/cm^2.

Still, the process, leading to the experienced phase-mismatch, needs to be discussed. Possible reasons are wavefront deformations and changes in the laser parameters in dependence of the pulse energy. Else, the process takes place inside the crystals and is not respected within the simulation.

Thinking of the latter, a phase-mismatch induced by self-heating due to absorption comes into mind. Its dependence on the pulse energy is obvious and an influence on the conversion efficiency was for example shown by Sabaeian [42]. The phase-mismatch Δk, induced by a temperature mismatch δT, is described by:

$$\Delta k = \frac{\delta T}{\Delta T} \tag{6.2}$$

where ΔT is the temperature acceptance bandwidth [52]. In KTP crystals, the amplitude of the temperature profile on the exit facet during second harmonic generation was measured to be 5.0±0.2 K (at a fluence of 2 J/cm^2), whereas no temperature gradient or less than 50 mK was detected in BiBO crystals (see also the experiments at SHG with the infrared camera, section 4.2.2). Since temperature acceptance bandwidth for KTP crystals is by a factor 10 higher than in BiBO crystals (24 K vs 2.2 K, see table 3.1) and the measured temperature mismatch is at least by a factor 100 higher than in BiBO crystals, the resulting temperature induced phase-mismatch is by a factor 10 higher in KTP crystals than in BiBO crystals. But on the contrary, the phase-mismatch, artificially introduced in the simulation, was identical for both crystals.

By comparing simulation and experiment, we conclude, that the self-heating was

Figure 6.3: Simulated conversion efficiency at third harmonic generation for a combination of two BiBO crystals. Maximum conversion efficiency is calculated to be 56 % at a fluence of 0.65 J/cm^2 and was experimentally determined to be 48 % at a fluence of 0.75 J/cm^2.
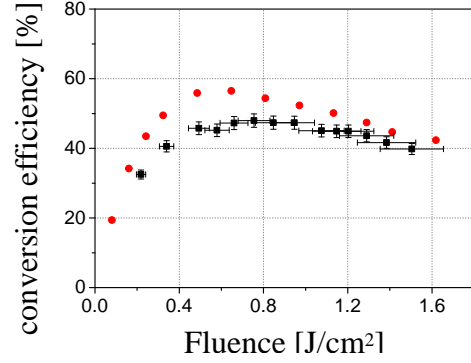
not the limiting factor for the experimentally realized conversion efficiency. Other influences, as crystal impurities or laser parameters like wavefront deformations play a dominating role. In a follow-up study, the influence of the wavefront at the fundamental wavelength on frequency conversion efficiency will be studied therefore.

The same applies for the simulation at third harmonic generation. There as well, the experimentally realized conversion efficiency matches the simulation, when the energy dependent phase-mismatch is respected. The calculated maximum conversion efficiency is 56 % at a fluence of 0.65 J/cm^2 and was experimentally determined to be 48 % at a fluence of 0.75 J/cm^2 (see figure 6.3).

7 Discussion

In the course of this Diploma thesis, an experimental set-up to investigate frequency conversion with nonlinear optical crystals was built. It allows to measure the conversion efficiency and also to investigate thermal lensing in the nonlinear crystals. Herein, a method to detect the occurrence of gray-tracking in situ during frequency conversion is demonstrated. All investigations were conducted in the background of a potential space application. The obtained data are discussed within this big picture in the following section. Finally, a conclusion is drawn.

7.1 Evaluation of experiments and simulations

First of all, the realized conversion efficiency will be discussed. It was as high as 76 ± 3 % at second harmonic generation with an anti-gray-tracking KTP crystal and a BiBO crystal, and as high as 48 ± 2 % at third harmonic generation, using a combination of two BiBO crystals. As stated in section 2.1.2, the aim was a conversion efficiency at THG of at minimum 30 %, which can be said to be fulfilled. For comparison, a study conducted with LBO crystals, which are preferred by the European Space Agency at the moment, can be considered. There, a conversion efficiency of 56 % was realized for SHG and of 34 % for THG [7]. Hence, the tested BiBO and KTP crystals are very promising candidates for space missions, when regarding the conversion efficiency.

In the following, the named drawbacks of the crystals, like small temperature acceptance bandwidth in BiBO crystals and gray-tracking in KTP crystals (see section 3.1), were to investigate. A longterm experiment, simulating one percent of the mission's planned operational time, was therefore conducted. No decrease

in conversion efficiency was found and variations were less than 1 % at second harmonic generation in KTP and BiBO crystals and less than 2 % at third harmonic generation with the BiBO crystals. Temperature control of the crystals is demonstrated to be sufficiently accurate to account for the small temperature acceptance bandwidth in BiBO crystals.

In KTP crystals, the occurrence of gray-tracking was detected during longterm operation and the resulting thermal lensing and its development over time could be monitored. Herefore, an indirect method, which is based on measuring the wavefront deformation of a co-aligned HeNe laser, was developed. Using this method, the formation and exponential saturation of color centers in the KTP crystal was observed in situ. Laser calorimetry, conducted before and after longterm operation, as well as after heating the crystal, confirmed the observations.

The noticed gray-tracking in KTP crystals could be of importance for its application in a spaceborne laser system. Although no significant influence on the conversion efficiency was discovered, the resulting thermal lensing and especially its changing over time could turn out to be of impact onboard a satellite. Since no readjustment of the optical components is possible when the satellite is operating in the Earth's orbit. In contrast to the investigated anti-gray-tracking KTP crystal, no such effect was detected in the BiBO crystals. Especially, the absorption at the second harmonic turned out to be less in BiBO than in KTP crystals. No relevant self-heating of the BiBO crystal during second harmonic generation was revealed. Neither when monitoring the crystal's surface temperature with an IR-camera, nor when inspecting the wavefront of the co-aligned HeNe laser with a Shack-Hartmann sensor, such an effect was over measurement threshold.

Apart from this, the laser calorimetric study (chapter 5) of the linear absorption coefficients unfold the excellent optical quality of the investigated BiBO crystals. Although the laser calorimetry was conducted at a wavelength of 940 nm and not at the fundamental wavelength (1064 nm) or its harmonic wavelengths, it allows to conclude on the optical quality and to compare absorption coefficients of the different crystals investigated. Absorption coefficients in BiBO crystals were as low as 40±10 ppm/cm (THG crystal) and 60±10 ppm/cm (SHG crystal) and were in the same range as the absorption coefficient of a LBO crystal (84±10 ppm/cm). Also here, the investigated KTP crystal showed higher absorption, already before

longterm exposition (810±10 ppm/cm).

As discussed in section 3.1, a disadvantage of BiBO crystals could be the lower laser induced damage threshold when compared to LBO crystals. It was determined for coated thin slices of BiBO crystals at the Institute of Technical Physics (DLR) to be 2.5±0.4 J/cm^2 at a wavelength of 532 nm and to be 4.1±0.5 J/cm^2 at a wavelength of 532 nm. Since damage occurred on the coatings and not in the bulk in these studies, different coating techniques or an optimization might allow for higher damage thresholds in BiBO crystals as well. Nevertheless, LBO crystal's damage threshold of 35.4±5.1 J/cm^2 at a wavelength of 1064 nm and 10.3±1.5 J/cm^2 at a wavelength of 532 nm needs to considered as a positive aspect of LBO crystals.

The Diploma thesis is completed with the numerical evaluation of the conducted experiments (chapter 6). Not only the crystal data, but also laser parameters like beam profile, divergence of the laser beam or pulse width and shape, are considered in the simulations. Hereby, the experimental situation is represented the best possible. For fluences below 2 J/cm^2 for the KTP crystal and below 1.5 J/cm^2 for BiBO crystals, simulation is in line with the experiment and conversion efficiency does not differ more than 5 %. At higher fluences, back conversion becomes more and more important in the experiment and the conversion efficiencies decreased with an increasing pulse energy in this regime. However, the process leading to this observed decreasing in conversion efficiency, is not respected within the simulations. To account for it, an artificial (energy dependent) phase-mismatch was introduced in the simulation. When it is respected, simulated and experimentally realized frequency conversion are equivalent. The maximum conversion efficiency does not differ by more than 5 % at SHG and than 8 % at THG between simulation and experiment.

Self-heating was supected to be the process causing the energy-dependent phase-mismatch. But self-heating was observed in KTP crystals and not in BiBO crystals during second harmonic generation (Chapter 4). In contrast to this, the above mentioned phase-mismatch had to be introduced for both crystals in the simulation. We therefore assume, that other processes, probably dependent on the parameters of the laser light at the fundamental frequency, play a dominant role in the experiments.

In a follow-up, the influence of the fundamental laser light's wavefront on the conversion efficiency will be studied therefore.

7.2 Conclusion

A frequency conversion unit, based on two BiBO crystals in a crystal holder suitable for a future space mission, is presented within this work. Conversion efficiency at second harmonic generation followed by sum frequency generation was realized to be as high as 48±2 %, converting the fundamental radiation in the infrared at a wavelength of 1064 nm to a radiation in the ultraviolet at a wavelength of 355 nm. The realized conversion efficiency overcomes studies conducted in the past and fulfills the requirements as stated by the European Space Agency. Further on, the conducted experiments like laser calorimetry and detection of wavefront deformations during frequency conversion, as well as a longterm experiment, revealed the excellent optical properties of the BiBO crystals. A potential drawback of BiBO crystals could be the lower damage threshold when compared to LBO crystals and further research needs to be conducted on this topic.

In KTP crystals, highly efficient generation of second harmonic radiation at a wavelength of 532 nm and a conversion efficiency of 76±3 % was demonstrated. A method to detect gray-tracking in situ is presented within this thesis and the formation of color centers during longterm operation is observed. It is revealed that the gray-tracking could be a limiting factor for a spaceborne application due to the change in absorption and the resulting changes in thermal lensing.

List of Tables

List of Figures

Bibliography

[1] Baseline aeolus measurement geometry, Apr. 2014. URL `http://www.esa.int/spaceinimages/Images/2005/06/Baseline_Aeolus_measurement_geometry`.

[2] J. A. Armstrong, N. Bloembergen, J. Ducuing, and P. S. Pershan. Interactions between Light Waves in a Nonlinear Dielectric. *Phys. Rev.*, 127:1918–1939, 1962.

[3] E. S. Bahaa and M. C. Teich. *Fundamentals of Photonics*. Wiley, 2nd edition, 2007. ISBN 978-0-471-35832-9.

[4] B. Boulanger, I. Rousseau, J.-P. Feve, M. Maglione, B. Menaert, and G. Marnier. Optical studies of laser-induced gray-tracking in KTP. *Quantum Electronics, IEEE Journal of*, 35(3):281–286, 1999.

[5] R. W. Boyd. *Nonlinear Optics*. Academic Press, 3rd edition, 2008. ISBN 0123694701, 9780123694706.

[6] C. Chen, Y. Wu, A. Jiang, B. Wu, G. You, R. Li, and S. Lin. New nonlinear-optical crystal: LiB_3O_5. *J. Opt. Soc. Am. B*, 6(4):616–621, 1989.

[7] A. Ciapponi, W. Riede, G. Tzeremes, H. Schröder, and P. Mahnke. Non-linear optical frequency conversion crystals for space applications. In *Photonic West*, San Francisco, USA, January 2011. SPIE.

[8] A. Ciapponi, H. Schröder, and W. Riede. Non-linear laser crystal development for frequency conversion. Technical Report 21747/08/NL/EM, Institute of Technical Physics, DLR, Stuttgart, Germany, March 2011.

[9] P. Clissold, E. Andersson, A. Dabas, M. Endemann, P. Ingmann, E. Källén, D. Offiler, and A. Stoffelen. ADM-Aeolus Science Report SP-1311. Technical report, ESA, ESTEC, Noordwijk, The Netherlands, 2008.

[10] Coherent Laser Group. *Operator's Manual The Coherent Infinity^{TM} Nd:YAG Laser System*, P/N: 0167-433-00, Revision B edition, 1998.

[11] J. Eichler, L. Dünkel, and B. Eppich. Die Strahlqualität von Lasern – Wie bestimmt man Beugungsmaßzahl und Strahldurchmesser in der Praxis? *Laser Technik Journal*, 1(2):63–66, 2004.

[12] D. Eimerl, S. Velsko, L. Davis, and F. Wang. Progress in nonlinear optical materials for high power lasers. *Progress in Crystal Growth and Characterization of Materials*, 20(1–2):59 – 113, 1990.

[13] M. Endemann. The ADM-Aeolus Mission. In *Proc. '6th Internat. Conf. on Space Optics'*, Noordwijk, The Netherlands, June 2006. ESTEC.

[14] M. Endemann. ALADIN TxA; A spaceborne UV laser. In *Conference on Lasers and Electro-Optics (CLEO)*, Baltimore, USA, May 2011.

[15] T. Y. Fan, C. E. Huang, B. Q. Hu, R. C. Eckardt, Y. X. Fan, R. L. Byer, and R. S. Feigelson. Second harmonic generation and accurate index of refraction measurements in flux-grown $KTiOPO_4$. *Appl. Opt.*, 26(12):2390–2394, 1987.

[16] P. A. Franken, A. E. Hill, C. W. Peters, and G. Weinreich. Generation of optical harmonics. *Phys. Rev. Lett.*, 7:118–119, Aug 1961.

[17] E. Goodwin and J. Wyant. *Field Guide to Interferometric Optical Testing*. SPIE field guides. SPIE, Berlingham, WA, 2006. ISBN 9780819465108.

[18] M. Hass. Measurement of very low optical absorption coefficients in bulk materials. *Optical Engineering*, 17(5):175525–175525–, 1978.

[19] H. Hellwig, J. Liebertz, and L. Bohatý. Linear optical properties of the monoclinic bismuth borate BiB_3O_6. *Journal of Applied Physics*, 88(1):240–244, 2000.

[20] Imagine Optic Inc. *The HASO Manual*, MAN-221199GDAa edition, 2000.

[21] ISO 11551. Prüfverfahren für den Absorptionsgrad von optischen Laserkomponenten (ISO 11551:2003); Deutsche Fassung , 2003.

[22] W. Koechner. *Solid-State Laser Engineering*. Springer Series in Optical Sciences. Springer, 2006. ISBN 9780387290942.

[23] P. Koepke and M. Sachweh. *Satellitenmeteorologie*. UTB GmbH, Stuttgart, 2012. ISBN 978-3-8385-3525-8.

[24] R. A. Kumar. Borate crystals for nonlinear optical and laser applications: A review. *Journal of Chemistry*, 2013. Article ID 154862.

[25] R. G. Lane and M. Tallon. Wave-front reconstruction using a Shack–Hartmann sensor. *Appl. Opt.*, 31(32):6902–6908, Nov 1992.

[26] E. M. LEVIN and C. L. MCDANIEL. The System Bi2O,—B2O3. *Journal of the American Ceramic Society*, 45(8):355–360, 1962.

[27] G. Mann. *Experimentelle und theoretische Untersuchungen zur Frequenzkonversion von Nd:YAG-Laserstrahlung mit hoher Durchschnittsleistung*. PhD thesis, Technische Universität Berlin, 2003.

[28] J. D. Mansell, J. Hennawi, E. K. Gustafson, M. M. Fejer, R. L. Byer, D. Clubley, S. Yoshida, and D. H. Reitze. Evaluating the Effect of Transmissive Optic Thermal Lensing on Laser Beam Quality With a Shack-Hartmann Wave-Front Sensor. *Appl. Opt.*, 40(3):366–374, 2001.

[29] U. Marksteiner, O. Reitebuch, S. Rahm, I. Nikolaus, C. Lemmerz, and B. Witschas. Airborne direct-detection and coherent wind lidar measurements along the east coast of Greenland in 2009 supporting ESA's Aeolus mission. In *Lidar Technologies, Techniques, and Measurements for Atmospheric Remote Sensing VII*, volume 8182, pages 81820J–81820J–8, Prague, Czech Republic, September 2011. SPIE.

[30] B. Martinez, V. Beau, S. Chico, S. Mainguy, and J. L. Rullier. Numerical and experimental study of focal spot degragation induced by particles on surface

optics. In *Laser-Induced Damage in Optical Material*, volume 6403, pages 64030F–64030F–9. SPIE, September 2006.

[31] D. Meschede. *Optik, Licht und Laser*. Teubner Studienbücher. Vieweg+Teubner Verlag, 2008. ISBN 9783835101432.

[32] D. N. Nikogosyan. *Newly Developed and Perspective Crystals*, chapter 6, pages 215 – 218. Springer, Wien, 2009. ISBN 0-387-22022-4.

[33] D. N. Nikogosyan. *Basic Nonlinear Optical Crystals*, chapter 2, pages 5 – 75. Springer, Wien, 2009. ISBN 0-387-22022-4.

[34] V. Petrov, M. Ghotbi, O. Kokabee, A. Esteban-Martin, F. Noack, A. Gaydardzhiev, I. Nikolov, P. Tzankov, I. Buchvarov, K. Miyata, A. Majchrowski, I. Kityk, F. Rotermund, E. Michalski, and M. Ebrahim-Zadeh. Femtosecond nonlinear frequency conversion based on BiB_3O_6. *Laser Photonics Reviews*, 4(1):53–98, 2010.

[35] B. C. Platt et al. History and principles of shack-hartmann wavefront sensing. *Journal of Refractive Surgery*, 17(5):S573–S577, 2001.

[36] O. Reitebuch and B. Witschas. Atmosphärenphysik - Über den Wolken. *Physik Journal*, 13:25–31, Mai 2014.

[37] O. Reitebuch, C. Lemmerz, E. Nagel, U. Paffrath, Y. Durand, M. Endemann, F. Fabre, and M. Chaloupy. The Airborne Demonstrator for the Direct-Detection Doppler Wind Lidar ALADIN on ADM-Aeolus: I Instrument Design and Comparison to Satellite Instrument. *Journal of Atmospheric and Oceanic Technology*, 26:2501–2515, 2009.

[38] O. Reitebuch, C. Lemmerz, U. Marksteiner, S. Rahm, and B. Witschas. Airborne lidar observations supporting the adm-aeolus mission for global wind profiling. In *26th Int. Laser Radar Conference ILRC*, pages 759–762, Porto Heli, Greece, Juni 2012.

[39] W. Riede, P. Allenspacher, M. Lammers, D. Wernham, A. Ciapponi, C. Heese, L. Jensen, H. Maedebach, S. Schrameyer, and D. Ristau. From ground to

space: how to increase the confidence level in your flight optics. In *Laser-Induced Damage in Optical Materials*, volume 8885, pages 88850D–88850D–9. Proc. SPIE, 2013.

[40] D. Roberts. Simplified characterization of uniaxial and biaxial nonlinear optical crystals: a plea for standardization of nomenclature and conventions. *Quantum Electronics, IEEE Journal of*, 28(10):2057–2074, Oct 1992.

[41] H. Rutt. Technical note 02-053: The thermal conductivity of macor at intermediate cryogenic temperatures. Technical report, Thomas Jefferson National Accelerator Facility, December 2002. URL `http://eprints.soton.ac.uk/264180/`.

[42] M. Sabaeian, L. Mousave, and H. Nadgaran. Investigation of thermally-induced phase mismatching in continuous-wave second harmonic generation: a theoretical model. *Opt. Express*, 18(18):18732–18743, 2010.

[43] H. Schröder, P. Wagner, D. Kokkinos, W. Riede, and A. Tighe. Laser-induced contamination and its impact on laser damage threshold. In *Laser-Induced Damage in Optical Materials*, volume 8885, pages 88850R–88850R–9. Proc. SPIE, 2013.

[44] M. P. Scripsick, D. N. LoIacono, J. Rottenberg, S. H. Goellner, L. E. Halliburton, and F. K. Hopkins. Defects responsible for gray tracks in fluxgrown $KTiOPO_4$. *Applied Physics Letters*, 66(25):3428–3430, 1995.

[45] Z. Shuqing, H. Chaoen, and Z. Hongwu. Crystal growth and properties of lithium triborate. *Journal of Crystal Growth*, 99(1–4, Part 2):805 – 810, 1990. ISSN 0022-0248.

[46] K. Strain, K. Danzmann, J. Mizuno, P. Nelson, A. Rüdiger, R. Schilling, and W. Winkler. Thermal lensing in recycling interferometric gravitational wave detectors. *Physics Letters A*, 194(1–2):124 – 132, 1994.

[47] D. M. Topa. Wavefront reconstruction for the Shack-Hartmann wavefront sensor. In *Optical Design and Analysis Software II*, volume 4769, pages 101–115, Seattle, Washington, July 2002. Proc. SPIE.

[48] N. Umemura, K. Miyata, and K. Kato. New data on the optical properties of BiB_3O_6 . *Optical Materials*, 30(4):532 – 534, 2007.

[49] S. P. Velsko, M. Webb, L. Davis, and C. Huang. Phase-matched harmonic generation in lithium triborate (LBO). *Quantum Electronics, IEEE Journal of*, 27(9):2182–2192, 1991.

[50] V. Wesemann, J. L'huillier, L. Friess, P. v. Loewis of Menar, G. Bitz, A. Borsutzky, R. Wallenstein, T. Salva, S. Vernay, and D. Rytz. Optical properties of BiB_3O_6 with different phase matching orientations. *Applied Physics B*, 84 (3):453–458, 2006.

[51] U. Willamowski, D. Ristau, and E. Welsch. Measuring the absolute absorptance of optical laser components. *Appl. Opt.*, 37(36):8362–8370, 1998.

[52] S. Wu, G. A. Blake, S. Sun, and J. Ling. A multicrystal harmonic generator that compensates for thermally induced phase mismatch. *Optics Communications*, 173(1–6):371 – 376, 2000.

[53] S. Yoshida, D. H. Reitze, D. B. Tanner, and J. D. Mansell. Method for measuring small optical absorption coefficients with use of a Shack–Hartmann wave-front detector. *Applied optics*, 42(24):4835–4840, 2003.

Eidesstaatliche Erklärung

Hiermit erkläre ich, Arne Potreck, geboren am 23.05.1984 in Leverkusen, dass ich die vorgelegte Diplomarbeit mit dem Titel: "Nonlinear Optical Frequency Conversion for Lasers in Space"' selbstständig und ohne fremde Hilfe verfasst habe. Alle verwendeten Quellen und sinngemäßen Zitate wurden gekennzeichnet und entsprechend angegeben.

Arne Potreck

Danksagung